Doctoral Dissertation (Censored)

博士論文（要約）

Experimental and Theoretical Study on Magnetism of $M_2Mo_3O_8$ (M=Mn, Fe) Epitaxial Thin Films

（$M_2Mo_3O_8$ (M=Mn, Fe)エピタキシャル薄膜の磁性に関する実験的及び理論的研究）

A Dissertation Submitted for the Degree of Doctor of Philosophy

December 2021

令和３年１２月博士（理学）申請

Department of Chemistry, Graduate School of Science,

The University of Tokyo

東京大学大学院理学系研究科化学専攻

Shishin Mo

毛　司辰

Abstract

1. Introduction

Multiferroic materials with simultaneous magnetic and ferroelectric orders have been eagerly studied because of their fascinating physics and future technological applications such as fast-writing, power-saving, and non-destructive data storage.

$M_2Mo_3O_8$ (M = 3d transition metal) is a promising multiferroic material due to its room-temperature ferroelectric polarization and magnetic-(electric-)field-induced modulation of polarization (magnetization) [1]. They also exhibit unique magnetic-field-induced magnetic phase transitions such as collinear ferrimagnetism (FR) to noncollinear spin-flop transition in $Mn_2Mo_3O_8$ and AFM to FR transition in $Fe_2Mo_3O_8$ [1,2]. However, for the practical applications, enhancement of their magnetic transition temperature (T_N) or generation of spontaneous magnetization (M_r) are demanded. Recently, epitaxial strain engineering has emerged as a powerful method for tuning the magnetism of oxide thin films. Although $M_2Mo_3O_8$ has not been prepared in thin film form so far, the epitaxial strain is expected to improve its magnetism. In my study, I investigated the synthesis process and epitaxial strain effect on ferroelectric polarization and magnetism of $Mn_2Mo_3O_8$ and $Fe_2Mo_3O_8$ thin films. The obtained films exhibited different magnetic orders from the bulk specimens, leading to a large spontaneous magnetization in $Mn_2Mo_3O_8$ films and FR in $Fe_2Mo_3O_8$ thin films. Moreover, the T_N values of the films were much higher than those of bulks.

2. Epitaxial strain-induced large spontaneous magnetization in $Mn_2Mo_3O_8$ thin films

Tensile-strain-induced $Mn_2Mo_3O_8$ thin films were fabricated on the Al_2O_3 (001) substrate. XPS and XAS measurements revealed that the film consists of Mo^{4+} and Mn^{2+} ions, similar to that in the case of bulk. From the cross-sectional STEM image of the film, Mo and Mn layers were clearly observed. From the atomic positions, the structural polarization was evaluated to be slightly larger than that of bulk which was also predicted by DFT calculations.

The in-plane remanent magnetization was more significant than the out-of-plane one, indicating in-plane magnetic anisotropy, which is in contrast to that in the case of bulk $Mn_2Mo_3O_8$. T_N was evaluated to be 108 K, which is more than two times higher than that of bulk (41 K) [2]. To explain the origin of the sizeable spontaneous magnetization of the film, I proposed a non-collinear spin model. In the model, the directions of tetrahedral (*tetra*-) and octahedral (*octa*-) Mn^{2+} spins are canted from the *c*-axis with different orientations, resulting in a non-collinear spin order. To support the model, I performed DFT calculations. Dzyaloshinskii-Moriya (DM) interaction coefficient was much smaller than others, indicating that the influence of DM interaction on the magnetism of $Mn_2Mo_3O_8$ is negligibly small. On the other hand, under the competition between nearest-neighbor exchange interaction and single-ion anisotropy, a noncollinear spin structure becomes most stable at 3 % in-plane strain, whereas collinear spin order is the most stable at 0 % strain.

3. Epitaxial strain control of crystal domains and magnetism of $Mn_2Mo_3O_8$ thin films

$Mn_2Mo_3O_8$ thin films, exhibiting magnetic and spontaneous ferroelectric orders simultaneously, were fabricated on yttria-stabilized zirconia (YSZ) (111) and Al_2O_3 (001) substrates. The films have hexagonal structures with a *c*-axis orientation. In the film on YSZ (111), two types of in-plane crystal domains appeared (*CD*1 and *CD*2), unlike the film on Al_2O_3. The *CD*1 (*CD*2) has the a-axis parallel (vertical) to the $[11\text{-}2]_{YSZ}$ direction. The volume fraction (V_f) of *CD*2 was controllable in an extensive range of 2−48 % by changing the film thickness. Large V_f of *CD*2 was obtained when the thickness was above 52 nm. In addition, the size of the crystal domains was also variable from 0.3 to >25 μm2 by changing the thickness. Such unique film growth is derived from the crystal structure of $Mn_2Mo_3O_8$, in which Mn and Mo layers are alternately stacked along the *c*-axis, and Mn_6 and Mo_6 hexagons in the layers are rotated 30° from each other. Furthermore, the increase in V_f of *CD*2 resulted in an increase of the magnetic transition temperate, probably related to the emergence of the crystal domain boundaries.

4. Antisite-driven high-T_N ferrimagnetism in $Fe_2Mo_3O_8$ thin films

I fabricated epitaxial $Fe_2Mo_3O_8$ thin films on various substrates, Al_2O_3(001) and $SrTiO_3$(111). The films exhibited ferrimagnetism with perpendicular anisotropy below magnetic transition temperature (T_N) of 230 K. This behavior is quite different from bulk which shows antiferromagnetic (AFM) behavior with T_N of 60 K [1]. For understanding the spin structure of the $Fe_2Mo_3O_8$ film, XMCD measurements were performed. It indicates that the sign of the sum of magnetic moments of *octa*-Fe^{2+} is opposite to that of *tetra*-Fe^{2+} and that the strength of the former is smaller than that of later; i.e., the ferrimagnetism is derived from the difference in the sum of magnetic moments between

tetra-Fe^{2+} and *octa*-Fe^{2+}.

From the STEM image of $Fe_2Mo_3O_8$ thin films, the occurrence of the antisite, the site exchange between Fe and Mo was obtained. To evaluate the effect of the antisite on magnetism, I performed DFT calculations. The result shows that antisite-induced structure cells prefer an in-plane tensile strain and an FR spin structure.

5. Conclusion

I successfully fabricated $Mn_2Mo_3O_8$ and $Fe_2Mo_3O_8$ thin films and modulated the magnetism. As for $Mn_2Mo_3O_8$, the spontaneous magnetization of the thin films was much larger than that in the case of the bulk, and the growth mode, which may affect the magnetism, can be controlled by changing the substrate and the thickness of the thin films. In the case of $Fe_2Mo_3O_8$, out-of-plane ferrimagnetism was obtained in the films, while the antiferromagnetism was obtained in bulk. In addition, T_N is enhanced in thin film form.

Acknowledgments

First of all, I would like to thank my supervisor, Prof. Tetsuya Hasegawa. He provided me with an excellent environment for both experimental and theoretical studies. Discussions with him are always full of help and fun. My works would have been impossible without his thoughtful help. My most profound appreciation goes to Prof. Tsukasa Katayama, who has provided me with considerable support in every moment of this research. His advice always helped me a lot.

I also owe my thesis to Prof. Akira Chikamatsu. Not only the measurement technique but also his charming talk always created a friendly and comfortable atmosphere in the laboratory. I would also like to express my gratitude to Prof. Yasushi Hirose, Dr. Shoichiro Nakao, and Mrs. Aya Imoji for their helpful comments on my research life in the Hasegawa laboratory.

I would like to send my sincere thanks to Mr. Shunya Tanaka, Mr. Ken Hayahara, Mr. Kuni Yamada, and Mr. Takuto Wakasugi. They entered the Hasegawa laboratory together with me when we were bachelor students. Their attitude toward the research is always encouraging me. I wish to thank them for being my good friends.

As a member of Katayama group, I am grateful for Katayama group members, Mr. Ke Gu, Mr. Kento Magara and Mr. Jun Kasahara, Mrs. Miki Takahashi. They provided me a comfortable environment to my research.

I would like to show my acknowledgment to the current and former members of the Hasegawa laboratory for their valuable comments in weekly meetings; Dr. Thantip S. Krasienapibal, Prof. Mayuko Oka, Dr. Tomoya Onozuka, Mr. Naoaki Hashimoto, Mr.

Koki Kawahara, Mr. Keisuke Yamada, Mr. Yusuke Suzuki, Mr. Toru Koizuki, Dr. Takahiro Maruyama, Dr. Michitaka Fukumoto, Mr. Takaaki Shiina, Mr. Jin Gou, Mr. Tsuchii Doi, Ms. Yuting Zhu, Mr. Gu Ke, Ms. Yannan Wang, Mr. Ryota Ishigami, Mr. Kento Magara, Mr. Jun Kasahara, Mr. Yo Nagashima, Mr. Takuma Nishimura, Mr. Yusuke Wakayama, Mr. Kazuya Okada, Mr. Koki Ogura, Mr. Hayato Suzuki, Ms. Miki Takahashi, Mr. Rei Kashima, Mr. Masao Goto.

I was supported by the Advanced Leading Graduate Course for Photon Science (ALPS), providing me with a scholarship and a variety of valuable programs for my doctoral course. Special thanks to Prof. Atsushi Fujimori, Prof. Shin-ichi Ohkoshi, Prof. Goro Shibata for continuing support in the ALPS course.

Finally, I would like to show my appreciation to my family for giving me the opportunity to learn in the Hasegawa laboratory.

December 2021

Shishin Mo

Contents

1 General introduction

1.1 Multiferroics

Multiferroic materials have been eagerly studied because of their fascinating physics and future technological applications such as fast-writing, power-saving, and non-destructive data storage (Fig. 1-1). The concept of "multiferroics" was proposed by H. Schmid in the 1990s, which was defined as materials that show two or more ferroic orderings (ferroelectricity, ferromagnetism, and ferroelasticity) in the same phase [3]. In this thesis, I focus on the combination of ferroelectric and ferromagnetic ordering. In general, the coexistence of ferroelectricity and ferromagnetism in the same material is still a big challenge because of the conflicting origins of these two orderings.

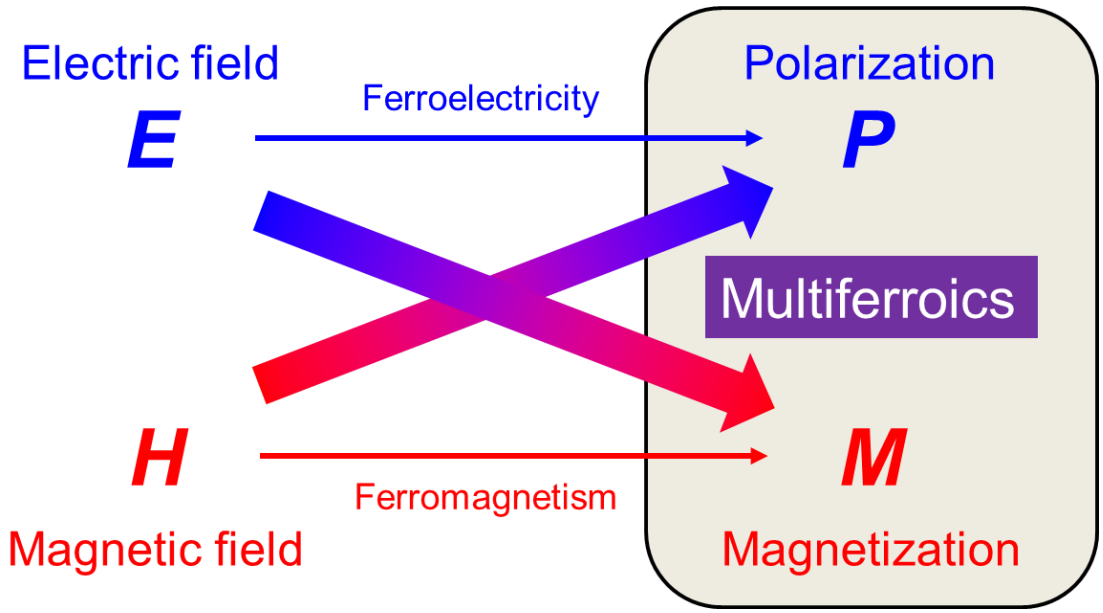

Figure 1-1. The definition of multiferroics.

1.1.1 Strict requirements of multiferroics

In order to obtain ferroelectricity, it is necessary to localize the electric dipole moment in the unit cell, and the direction of the moment needs to be aligned by dipole-dipole interaction, which generates the polarization. Usually, there are two conventional mechanisms for ferroelectricity based on two types of cations [4]: (1) d^0 cations, which make the repulsive Coulomb force small and are easily displaced from the center, *e.g.*, Ti^{4+} (2) cations with lone pair electrons, *e.g.*, Pb^{2+}. On the other hand, partially occupied *d* or *f* electrons are needed for ferromagnetism, and thus it is challenging to realize ferromagnetism in a simple metal oxide. Even in a perovskite, super-exchange interaction tends to lead to antiferromagnetism. As a consequence, it can be said that ferromagnetism and ferroelectricity are contrary to each other in *d* electrons.

1.1.2 Classification of multiferroics

Attempts have been made to overcome this "d^0-ness" requirement [4], and many multiferroic compounds have been discovered so far. They are traditionally classified into two types called type-I and type-II, as proposed by D. Khomskii [5].

1.1.2.1 Type-I multiferroics

Materials that show ferroelectricity and magnetism independently are referred to as type-I multiferroics. There are several approaches to realize two orderings: (1) superlattices of ferromagnetic and ferroelectric compounds (e.g., $(LuFeO_3)_9/(LuFe_2O_4)_1$ [6], $(1\text{-}x)(Ca,Sr)_{1.15}Tb_{1.85}Fe_2O_7/xCa_3Ti_2O_7$ [7], (2) single compounds in which ferroelectricity and ferromagnetism originate from different elements (e.g., $BiFeO_3$ [8], $EuTiO_3$ [9], *h*-$RMnO_3$ [10]). Because of the independence of

ferroelectricity and ferromagnetism, the critical temperatures (T_C for ferroelectricity and T_N for (anti)ferromagnetism) are different, and T_N is always much lower than T_C (Fig. 1-2).

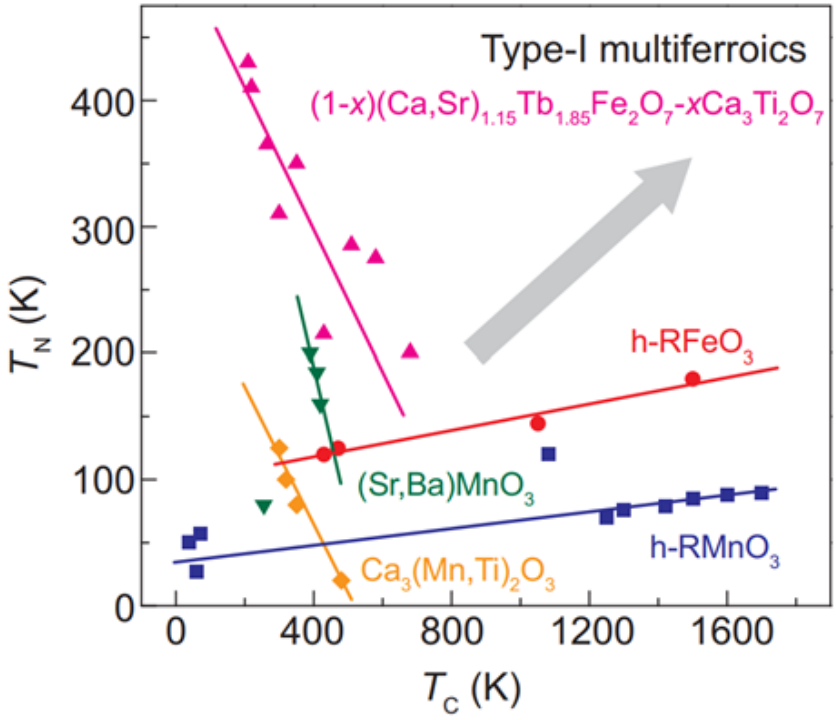

Figure 1-2. T_N and T_C of type-I multiferroics [11].

1.1.2.2 Type-II multiferroics

The term type-II multiferroic is for materials in which ferroelectricity arises from cations with partially filled *d* electrons. The type-II ferroelectricity is usually generated by specific magnetic order (Note it is natural to except $T_C = T_N$), which shows a substantial magnetoelectric response. However, as shown in Fig. 1-2, the critical temperature should be low to obtain large polarization. In general, three mechanisms for type-II multiferroics were proposed: (1) inverse Dzyaloshinskii-Moriya (DM) interaction (e.g., *o*-$TbMnO_3$ [12]), in which the polarization is generally tiny (<0.01 μC/cm^2); (2) exchange striction (e.g., *R*MnO_3 under an external pressure [13]), and (3) spin-dependent *p-d*

hybridization (e.g., $Ba_2CoGe_2O_7$ [7]). These mechanisms will be discussed in section 1.1.3.

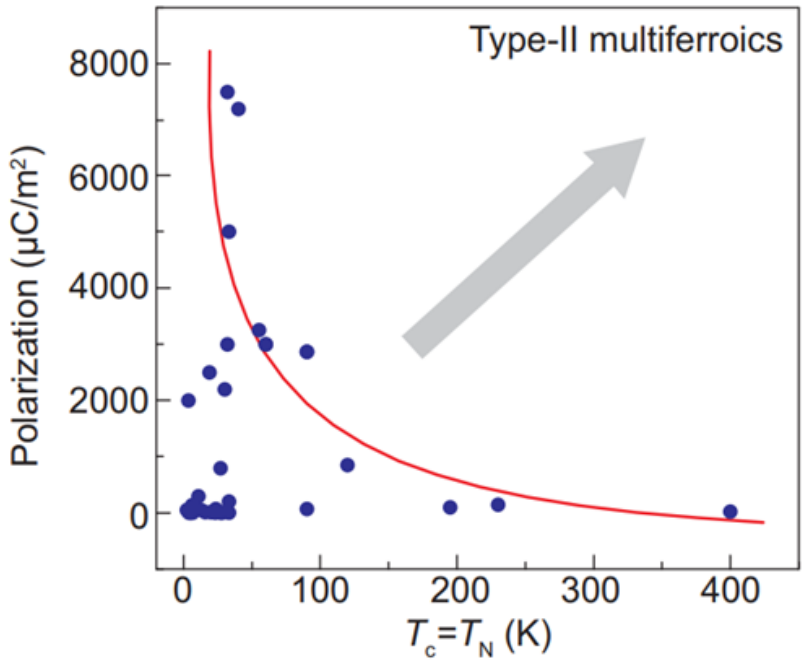

Figure 1-2. T_N, T_C, and polarization of type-II multiferroics [11].

1.1.2.3 Type-III multiferroics

Most recently, a new class of multiferroics based on polar magnet oxides, called type-III, was proposed by Ravi Shankar PN *et al.* [14]. The spontaneous ferroelectric polarization in this type of compound is derived from the polar crystal structure, which does not necessarily show a polar-nonpolar phase transition in contrast to type-I multiferroics (e.g., Ilmenite-type $MnTiO_3$, $MnTaO_2N$). In a polar magnet, the change of polarization (ΔP) can be controlled by an external magnetic field. The order of this magnetoelectric effect in type-III multiferroics is larger than type-I one because of the strong coupling. On the other hand, when compared with

type-II multiferroics, the noncentrosymmetric and polar structures are kept in the polar magnet regardless of the magnetic structure. This promises high-temperature multiferroicity because a complex magnetic structure usually emerges at low temperatures. Furthermore, the magnitude of the ferroelectric order in type-III multiferroics is typically much larger than that of type-II one.

1.1.2.4 Other multiferroic compounds

There are several exceptions which are difficult to be classified to type-I, type-II, or type-III: (1) non-d^0 ferroelectricity driven by second-order Jahn-Teller distortion (e.g., $BaMnO_3$ [15]), (2) non-d^0 ferroelectricity in metastable phase induced by epitaxial strain (e.g., $Sr_{0.5}Ba_{0.5}MnO_3$ [16]).

1.1.3 Magnetoelectricity in multiferroics

According to S. Dong *et al.* [17], magnetoelectricity can be provided by three couplings: spin-orbit coupling, spin-lattice (or called spin-phonon) coupling, and spin-charge coupling.

1.1.3.1 Spin-orbit coupling

The spin-orbit coupling, which is a relativistic effect connecting magnetic moments and charge dipoles, usually plays a significant role in magnetoelectricity in multiferroics. The spin-orbit coupling is seen as a form of Dzyaloshinskii-Moriya (DM) interaction [18,19]. The final form of the DM interaction can be expressed as:

$$H_{\mathrm{DM}} = \boldsymbol{D}_{ij} \cdot \left(\boldsymbol{S}_i \times \boldsymbol{S}_j\right), \qquad (\mathbf{1.1})$$

where $\boldsymbol{S}$ represents the spin vector and $\boldsymbol{D}$ is the coefficient vector, called the DM vector.

Since ***D*** is a vector, one needs to determine the direction of ***D***, which depends on the symmetry of the material. Moriya formulized this problem and listed five rules [19]mm:

(1) If the midpoint of atom *i* and *j* is an inversion center, ***D*** = 0.

(2) If there is a mirror plane that is perpendicular to line *ij* and passes through the midpoint of atom *i* and *j*, ***D*** is parallel to the mirror plane, or ***D*** is perpendicular to line *ij*.

(3) If a mirror plane passes atoms *i* and *j*, ***D*** is perpendicular to the mirror plane.

(4) If a two-fold rotation axis is perpendicular to line *ij* and passes through the midpoint of atoms *i* and *j*, ***D*** is perpendicular to the two-fold axis.

(5) If an *n*-fold axis ($n > 1$) passes through atom *i* and *j*, ***D*** is parallel to line *ij*.

By these Moriya's rules, the direction of ***D*** can be determined, and the contribution of spin-orbit coupling can be estimated. Furthermore, from equation 1.1, it is evident that the spin pairs prefer a canted spin state due to the cross-product between them. More important, by applying an external electric field (***E***), which can slightly change the structure and break the symmetry, the asymmetric configuration can be broken. Then, magnetization (***M***) emerges as a linear magnetoelectric response, *i.e.*, $\boldsymbol{M} \sim \alpha_{ME}\boldsymbol{E}$, where α_{ME} is the magnetoelectric coefficient. Such spin-orbit(-lattice) coupling works in most multiferroics.

1.1.3.2 Spin-lattice coupling

Since spin-orbit coupling is often accompanied by a change in the lattice, the pure spin-lattice coupling is described here. This is called the symmetric exchange striction, giving an alternative mechanism for magnetoelectricity. With a particular magnetic ordering, bond distortion may occur to gain energy by exchange

coupling between magnetic ions. In a centrosymmetric system, the distortion is canceled out by each other so that this magnetic-order-driven distortion produces electric polarization and finally realizes magnetoelectric coupling in a noncentrosymmetric system, e.g., *o*-$HoMnO_3$ [20] and Ca_3CoMnO_6 [21].

1.1.3.3 Spin-charge coupling

One of the approaches to obtain multiferroicity is to induce ferroelectricity in an (anti-)ferromagnetic material. Although there is no clear relationship between magnetism and polarization, charge ordering (charge density) can connect them and finally lead to magnetoelectricity. However, to modify a charge ordering, materials with relatively small bandgaps are needed. Such materials are usually associated with an experimental difficulty, i.e., sizeable current leakage. This type of coupling can be achieved in thin films or at interfaces/domain walls.

1.1.3.4 Other couplings

Without interatomic interaction, the single-site (with ligand around) effect has also been considered, called spin-dependent metal-ligand (*p*-*d*) hybridization [22], which can be expressed as below:

$$\Delta \boldsymbol{P} = \sum_i (\boldsymbol{e}_i \cdot \boldsymbol{S}_i)^2 \boldsymbol{e}_i.$$

Due to the hybridization associated with spin-orbit interaction, the charges of the metals (*M*) and ligands (*X*) vary with the angle *X*-*M*-*X* changing. As a result, the electric polarization $\Delta \boldsymbol{P}$ emerges between the metal cation and the ligand, resulting in ferroelectricity in a whole system. Moreover, the change of the angle *X*-*M*-*X* affects the double exchange interaction, which contributes to magnetism.

1.2 Multiferroic $M_2Mo_3O_8$

The synthesis of $M_2Mo_3O_8$ (M=Mg, Mn, Fe, Co, Ni, Zn, Cd) was first reported by McCarroll *et al*. in 1957 [23]. $M_2Mo_3O_8$ has a hexagonal structure, in which tetrahedral (*tetra*-) and octahedral (*octa*-) M layers and Mo trimer layers are alternately stacked along the *c*-axis [24]. The elongation and distortion of the MO_4 tetrahedra and the MO_6 octahedra break the inversion symmetry and lead to spontaneous ferroelectric polarization along the *c*-axis [24]. On the other hand, with magnetic M^{2+} ions, the magnetic ordering occurs in $M_2Mo_3O_8$ below T_N. Since Mo^{4+} ions are thought to form spin-singlet trimers and not contribute to the magnetism (Fig. A-3) [25], the magnetism of $M_2Mo_3O_8$ is dominated by the 3*d* electrons of M^{2+} ions, and a variety of magnetic states including collinear and complex noncollinear states have been found. There are two types of collinear spin states, ferrimagnetism, and antiferromagnetism. In a ferrimagnetic state, M^{2+} cations with the same coordination number are ferromagnetically coupled. Since the spins of the antiferromagnetically coupled *tetra*-M^{2+} and *octa*-M^{2+} cannot cancel each other perfectly due to the processional motion of the spins, a small magnetization can emerge at a finite temperature. On the other hand, in the antiferromagnetic state, the net magnetization of the M^{2+} cations with the same coordination number is zero, which results in completely zero magnetization in the compound. Since the ferroelectric polarization and the magnetic ordering coexist in $M_2Mo_3O_8$, magnetic $M_2Mo_3O_8$ is considered to be a type-III multiferroic compound [14]. In this section, I focus on $M_2Mo_3O_8$ with only one magnetic ion M and not with a mixture of different magnetic ions such as $Fe_xMn_{1-x}Mo_3O_8$ [2], $Fe_xZn_{1-x}Mo_3O_8$ [26], $MgNiMo_3O_8$ [27], *etc*.

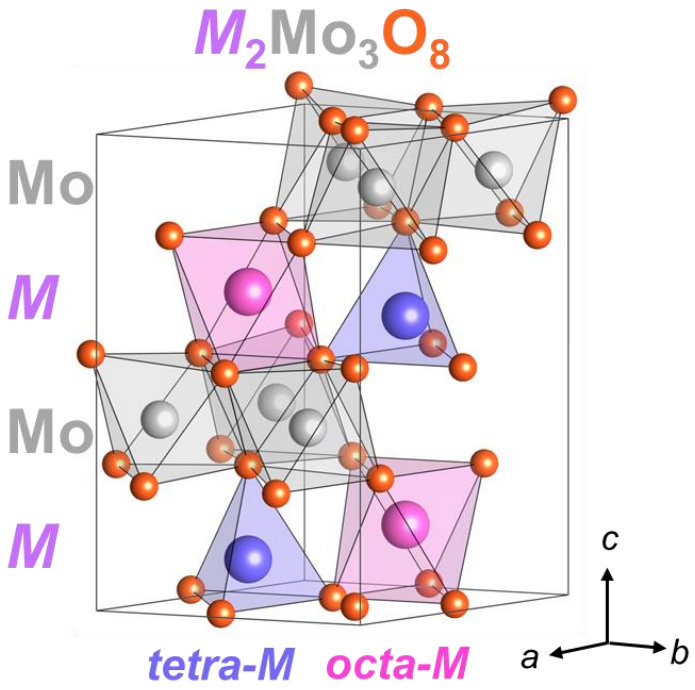

Figure 1-3. Crystal structure of $M_2Mo_3O_8$. The structure is written by VESTA [28].

Table 1-1. The most stable magnetic *H*-induced phases of magnetic $M_2Mo_3O_8$.

M	**Most stable phase**	**T_N (K)**	***H*-induced phase**	**Ref.**
Mn	FR // *c*-axis	41.5	Spin Flop	[2,29,30]
Fe	AFM	59.5	FR // *c*-axis	[26,31,32]
Co	AFM	39	Not reported	[33]
Ni	Noncollinear AFM	6	Spin Flop	[27,34]

1.2.1 $Mn_2Mo_3O_8$

$Mn_2Mo_3O_8$, also known as Isekite, exhibits L-type ferrimagnetism below T_N = 41 K [2], in which the magnetic moment at *octa*- and *tetra*-Mn^{2+} are canceled at zero temperature but not at finite temperature. Figure 1-4(a) shows the phase diagram of $Mn_2Mo_3O_8$. Mn^{2+} with high-spin configuration forms a half-filled 3*d* shells and results in an S=5/2 spin and an L=0 orbital moment, which means that the spin-orbital coupling is almost quenched, and a weak magnetic single-ion

anisotropy is only allowed via higher-order interactions [35]. First-principles calculations also revealed a weak DM interaction, leading to a positive single-ion anisotropy for *tetra*-Mn^{2+} and a negative single-ion anisotropy for *octa*-Mn^{2+}. Under a magnetic field, $Mn_2Mo_3O_8$ is transformed into a spin-flop state. The FR phase of $Mn_2Mo_3O_8$ shows the linear magnetoelectric response at the low-*H* region (Fig. 1-4(b)). The magnetoelectricity of $Mn_2Mo_3O_8$ is thought to be explained by the nonrelativistic exchange striction mechanism.

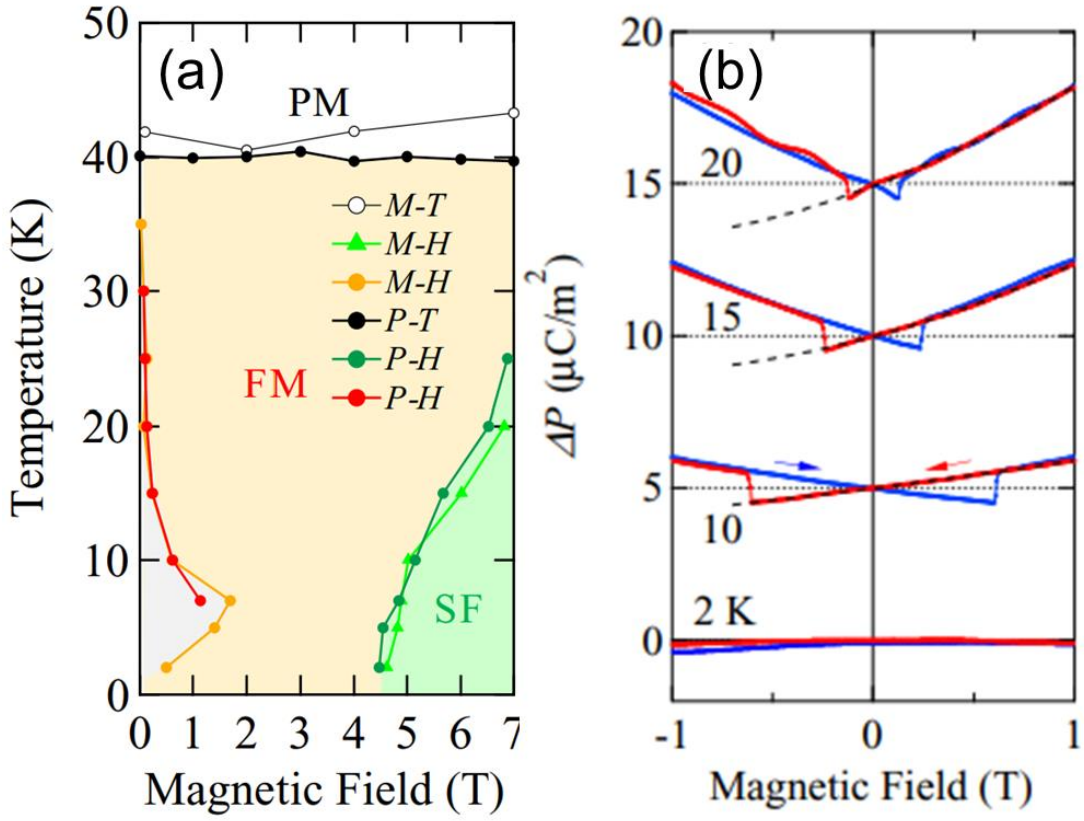

Figure 1-4. (a) *H-T* phase diagram. FM and SF represent ferrimagnetism and spin flop state, respectively. A gray region around the zero-field is the hysteretic region. (b) Magnified data for *H* dependence of *P* along the *c*-axis with *H* around (a) the lowest temperature. Reprinted figure with permission from Ref. [2]. Copyright 2021 by the American Physical Society.

1.2.2 $Fe_2Mo_3O_8$

$Fe_2Mo_3O_8$, also known as Kamiokite, is antiferromagnetic below T_N = 59.5

K with perpendicular anisotropy. As a promising multiferroic compound, magnetoelectric properties have been widely investigated. There are two types of magnetoelectric responses in $Fe_2Mo_3O_8$: One appears at the single magnetic phase, and the other appears at the *H*-induced AFM-FR transition. The former is based on the exchange-striction mechanism and the spin-dependent *d-p* hybridization mechanism, while the latter is only contributed by the exchange-striction mechanism. Theoretical calculations have also been performed to investigate the magnetic and electric structures of $Fe_2Mo_3O_8$ [25,31]. Consequently, it was revealed that the AFM–FR phase transition was triggered by the translocation of oxygen ions [25,31]. However, some inconsistencies were observed between the results of previous calculations and experiments. For example, it was theoretically predicated that AFM-$Fe_2Mo_3O_8$ would exhibit triclinic symmetry and that the hexagonal phase was energetically unstable and metallic [25], in contrast to experiments demonstrating an insulating state with a hexagonal structure [1,36]. Recently, Reschke *et al*. conducted density functional theory (DFT) calculations by considering spin-orbit coupling, and they reproduced the hexagonal structure with an insulating electronic state for AFM-$Fe_2Mo_3O_8$ [37], demonstrating the importance of the spin-orbit effect on the crystal and electric structures, although it was thought not to contribute to the magnetoelectricity [37].

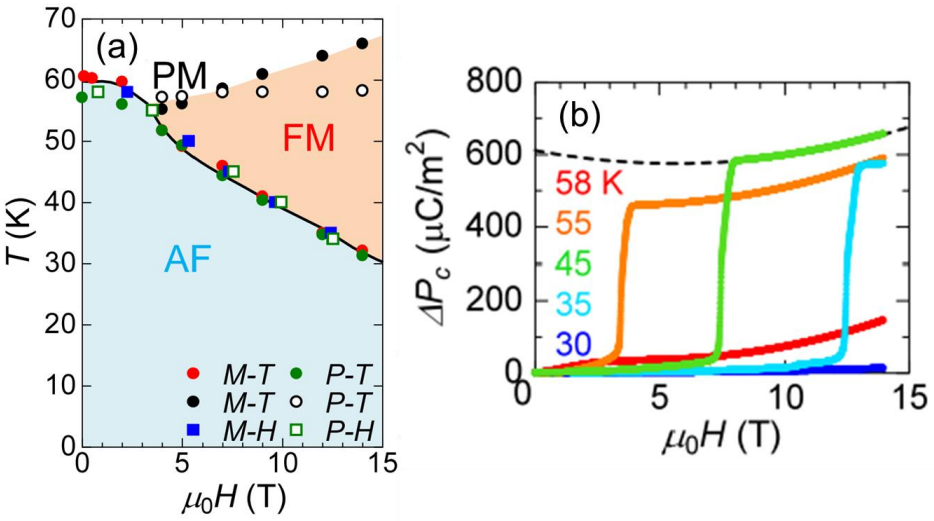

Figure 1-5. (a) *H-T* phase diagram. (b) *H-ΔP*$_C$ plots with different temperatures. These figures are reproduced with permission from Ref. [26]. Copyright 2021 by the American Physical Society. (Licensed under CC BY 3.0)

Recent works revealed that the spin-orbit effect on the Fe d^6 state is also essential for making $Fe_2Mo_3O_8$ a hexagonal insulator. The FeO_6 octahedron exhibits C_{3v} symmetry, not O_h because it is stretched along the *c*-axis. According to the symmetry reduction from O_h to C_{3v}, the t_{2g} orbital splits into a two-fold degenerate, e_g' and single a_{1g} orbitals [38], where the latter is occupied by an electron (Fig. 3(a)). By considering the spin-orbit effect, the e_g' bands are stabilized, and a gap opens between them. One electron occupies one of them. Furthermore, the FeO_4 tetrahedron exhibits C_{3v} symmetry owing to the stretch along the *c*-axis. In the *tetra*-Fe, two-fold degenerate *e* orbitals exhibit the lowest energy [39]. Without spin-orbit coupling, one spin-down electron resides in the two-fold degenerate *e* orbitals, as illustrated in Fig. 3(b), resulting in a finite DOS at E_F. However, the *e* orbitals are further split into two orbitals when the spin-orbit coupling is considered. The former orbital is filled by an electron, thereby forming a Mott gap and realizing a Mott insulator state. A calculation work with density of states can also be found in Appendix A.

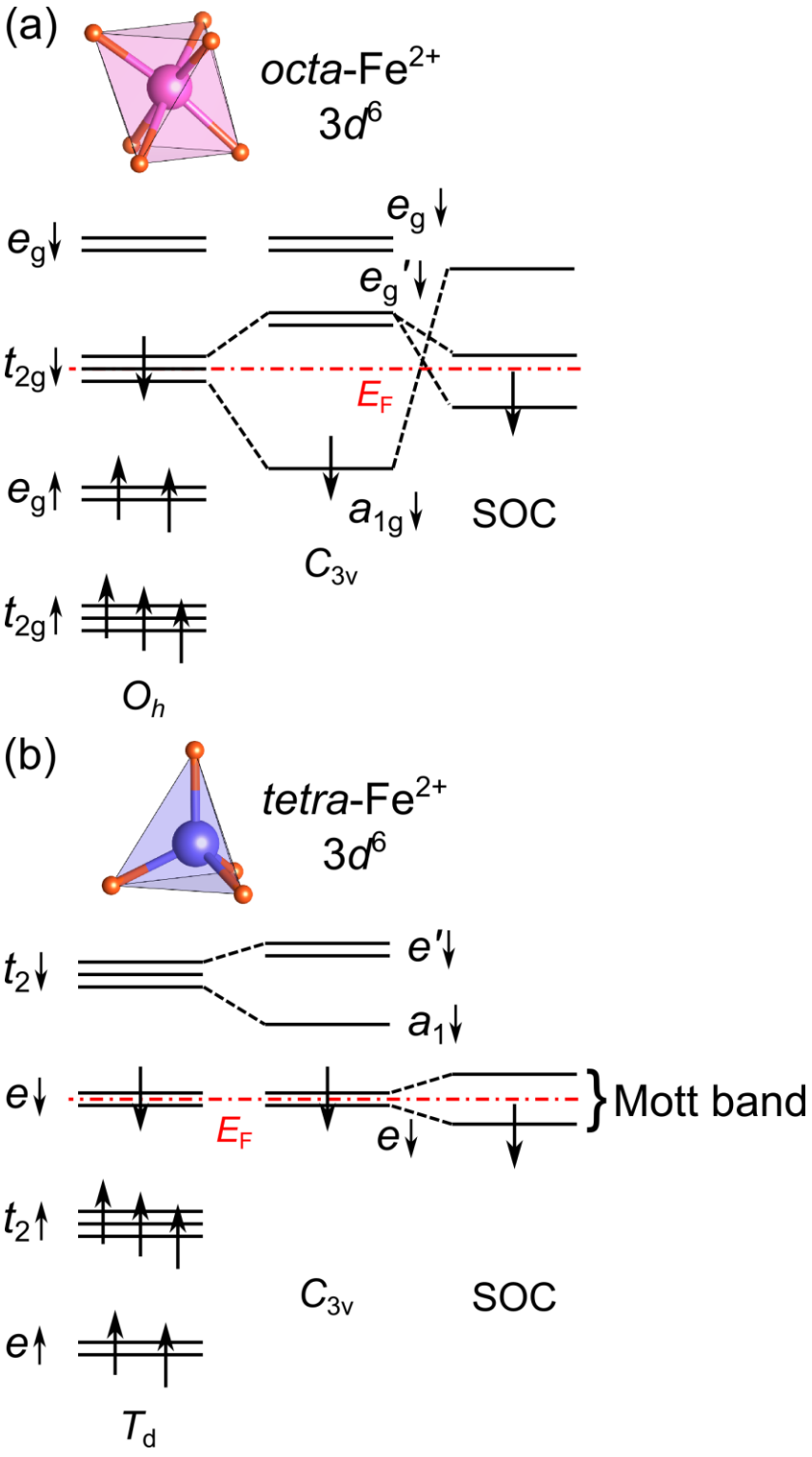

Figure 1-6. Band diagrams of (**a**) *octa*-Fe^{2+} and (**b**) *tetra*-Fe^{2+}.

1.2.3 $Co_2Mo_3O_8$ and $Ni_2Mo_3O_8$

The magnetism of the rest of magnetic $M_2Mo_3O_8$, $Co_2Mo_3O_8$ and $Ni_2Mo_3O_8$, has not yet been widely investigated. The ground states of AFM (T_N = 39 K) and a noncollinear AFM (T_N = 6 K) of $Co_2Mo_3O_8$ [33] [32] and $Ni_2Mo_3O_8$ [27,34], respectively, are well evidenced by neutron scattering. There is still no report on the field-induced magnetic transition of $Co_2Mo_3O_8$ and $Ni_2Mo_3O_8$. Performing a similar analysis as the band diagram of $Fe_2Mo_3O_8$, d^7 electrons of Co^{2+} fully fill the e_g' bands of *octa*-Co^{2+} and *e* bands of *tetra*-Co^{2+}, while d^8 electrons of Ni^{2+} fully fill the e_g' and a_{1g} bands of *octa*-Ni^{2+} and *e* and a_1 bands of *tetra*-Ni^{2+}. The magnetoelectricity in $Co_2Mo_3O_8$ is quite different from those in $Fe_2Mo_3O_8$ and $Mn_2Mo_3O_8$, which show only the second-order magnetoelectric effect allowed by the magnetic space group of $Co_2Mo_3O_8$, while the magnetoelectricity of $Ni_2Mo_3O_8$ is more complicated than that of other $M_2Mo_3O_8$, and the origin is still unclear.

1.3 Magnetism of metal oxide thin films

Transition metal oxides have been attracted wide attention for their variety of couplings among charge, orbital, spin, and lattice. A powerful method to modify their physical properties, especially magnetism, is thin film fabrication, where in-plane epitaxial strain from the substrate can be applied to the film. The modulation of magnetism by strain engineering is mainly achieved through the change of lattice constants, domain structures, and defect structures, which could appear both independently and simultaneously.

A well-known example for controlling the lattice constants is seen in $BiFeO_3$, a famous room-temperature multiferroic compound exhibiting a canted G-type AFM (M ~ 0.02 μ_B/Fe) in bulk $BiFeO_3$ [40]. $BiFeO_3$ thin films were fabricated on a variety of substrates, and their ferroelectric domains and antiferromagnetic spin textures were imaged with piezoresponse force microscopy and a scanning NV (nitrogen-vacancy) magnetometer, respectively (Fig. 1-7) [41]. The film shows a cycloidal spin order with an in-plane strain from -1.6% to +0.5%, while a canted AFM phase appears with an in-plane strain over +0.5%. In $LaCoO_3$, a low-spin state to a mixed intermediate-/high-spin state transition is induced by an approximate tensile strain of 1% [42]. The easy axis of $LaCoO_3$ films can be switched between in-plane and out-of-plane directions by using the strain [43]. X-ray linear dichroism (XLD) measurements obtained the decreasing $3z^2$-r^2 orbital occupancy of Co cations, which resulted in a weakening of the out-of-plane anisotropy.

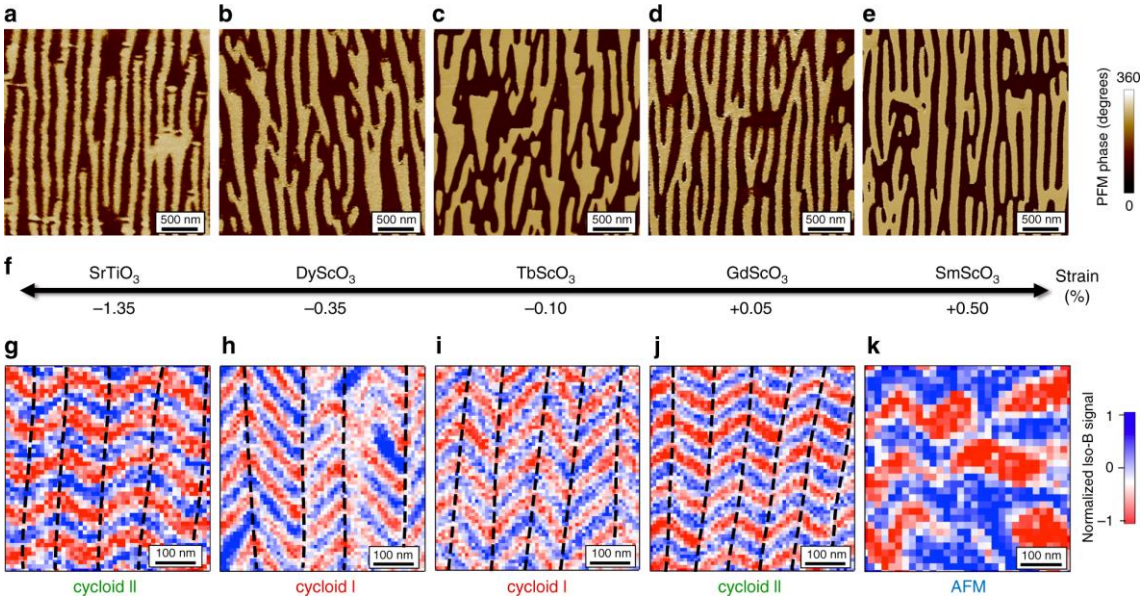

Figure 1-7. a–e In-plane PFM phase images of $BiFeO_3$ films grown on $SrTiO_3$ (a), $DyScO_3$ (b), $TbScO_3$ (c), $GdScO_3$ (d) and $SmScO_3$ (e) substrates. (f) Sketch of the evolution of the epitaxial strain in $BiFeO_3$ as a function of the substrate. (g–k) NV magnetometry images corresponding to the ferroelectric domains depicted in (a–e). The dashed lines in (g–j) are guides to the eyes, reflecting a change of the cycloid propagation vector associated with the ferroelectric domain walls. The symbol AFM in (k) stands for pseudo-collinear antiferromagnetic order. This figure is reproduced with permission from Ref. [41]. Copyright 2021 by Springer Nature. (Licensed under CC BY 4.0)

Modification of domain structure is also a practical approach to modify the physical properties. $Gd_{0.6}Ca_{0.4}MnO_3$ [44] is an example in which an in-plane strain from the substrates can influence the magnetism: On $SrLaAlO_3$ substrates, $Gd_{0.6}Ca_{0.4}MnO_3$ undergoes a compressive strain, and twin boundaries are formed in the film. The film shows a large coercive field, which can be explained by the pinning of domain boundaries. On the other hand, on $SrTiO_3$ and $(LaAlO_3)_{0.3}(Sr_2AlTaO_6)_{0.7}$ substrates where $Gd_{0.6}Ca_{0.4}MnO_3$ undergoes a tensile strain, only c-oriented films can be obtained. The film contains nanoclusters as the secondary phase, as observed by cross-sectional high-resolution transmission electron microscopy. The formation of the nanoclusters affects the ratio of Mn^{4+} and Mn^{3+} and the number of oxygen defects that suppress the magnetic double exchange

interaction and finally decrease the magnetization.

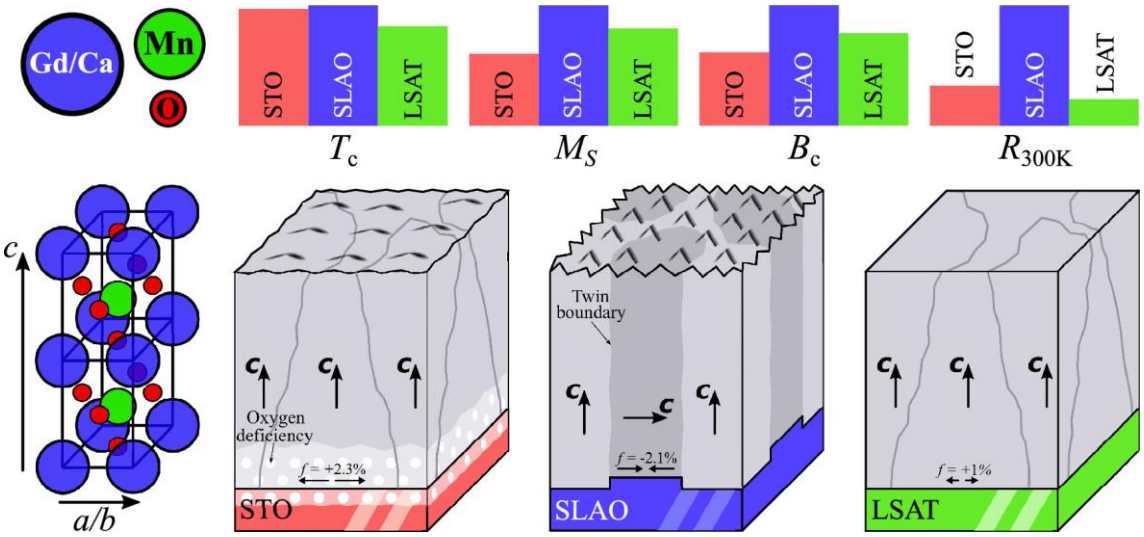

Figure 1-8. Domain orientations shown schematically for GCMO films grown on different substrates. The $Gd_{0.6}Ca_{0.4}MnO_3/SrTiO_3$ and $Gd_{0.6}Ca_{0.4}MnO_3/(LaAlO_3)_{0.3}(Sr_2AlTaO_6)_{0.7}$ films are *c*-oriented in the out-of-plane direction. The $Gd_{0.6}Ca_{0.4}MnO_3/ SrLaAlO_3$ has twinned domains with *c*-axis oriented in the out-of-plane and in-plane directions. The $Gd_{0.6}Ca_{0.4}MnO_3/SrTiO_3$ has oxygen deficiency in the interface region, which is shown by white dots. The *f* is the lattice mismatch between $Gd_{0.6}Ca_{0.4}MnO_3$bulk and the substrates. The bars show variations in Curie temperature (T_C), magnetization at 5 T (M_s), and resistivity at room temperature (R_{300}) in the films. This figure is reproduced with permission from Ref. [44]. Copyright 2021 The Authors. Published by American Chemical Society. (Licensed under CC BY 4.0)

Another important topic related to a strain-induced effect on magnetism is the role of defects, including oxygen vacancy (V_O), cation vacancy (V_C), and antisite defect. Among them, V_O has received considerable attention because of the easiness of introducing V_O. For example, inducing V_O in $YMnO_3$, $LaMnO_3$ films shows a transition from AFM to ferromagnetism (FM), depending on the amount of oxygen vacancy. In this case, V_O can change the *p-d* hybridization between Mn and O and thus affects the double exchange interaction, similar to the scenario described in section 1.1.3.4. The influence of V_C has scarcely been investigated compared to V_O, except for the studies on d^0 magnetism in metal oxide materials such as HfO_2, TiO_2,

and ZnO. There is still no report on the relationship between strain and V_C defects. Antisite defects have been studied in double perovskite oxides $A_2BB'O_6$ [45–51]. Among them, an excellent candidate material for novel spintronics and magnetoresistive applications is Sr_2FeMoO_6 [49–51], whose T_C for ferromagnetism in polycrystalline bulk Sr_2FeMoO_6 is far above the room temperature, about 450 K [50]. In Sr_2FeMoO_6 thin films, not only antisite defects but also compressive strain and V_O contribute to the magnetism [51]. As shown in Fig. 1-9, antisite defects and compressive strain lower T_N and saturate magnetization (M_S) while V_O enhances T_N and suppresses M_S. To my best knowledge, there is still no report on antisite-defect-driven enhancement of T_C or M_S.

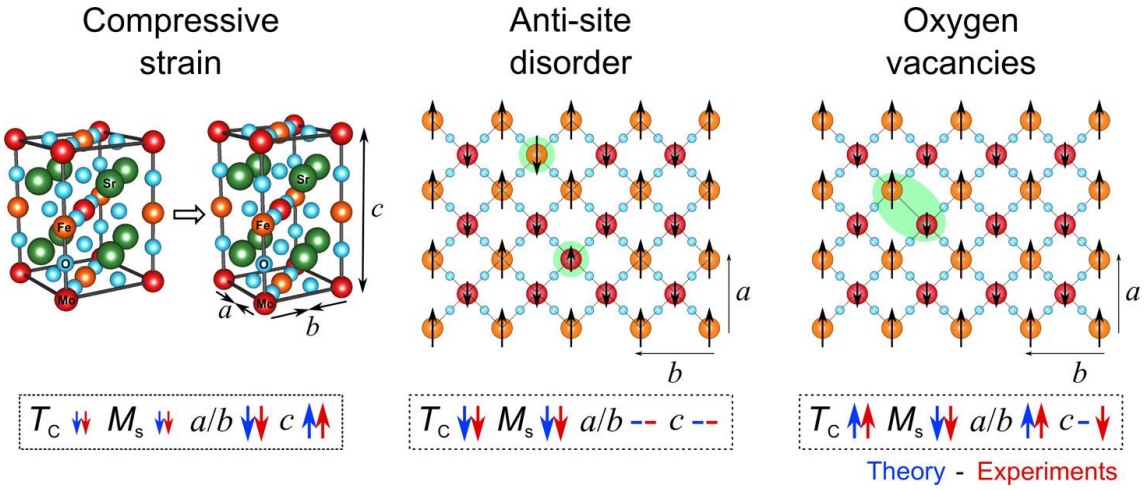

Figure 1-9. A schematic picture of the changes in Sr_2FeMoO_6 thin films caused by compressive strain, antisite disorder, and oxygen vacancies. The structural modifications due to these defects are illustrated at the top, and the changes in the main magnetic and structural properties from the experiments (red) and theoretical calculations (blue) at the bottom. The arrows imply the direction of change in the defect concentration range of the films, and the lines represent constancy. Reprinted with permission from Ref. [51]. Copyright 2021 American Chemical Society.

1.4 Purpose of the research

Multiferroic materials that have simultaneous magnetic and ferroelectric orders have been eagerly studied because of their fascinating physics and future technological applications such as fast-writing, power-saving, and non-destructive data storage. $M_2Mo_3O_8$ (M = 3d transition metal) is a promising multiferroic material due to its room-temperature ferroelectric polarization and magnetic-(electric-)field-induced modulation of polarization (magnetization) [1]. They also exhibit unique magnetic-field-induced magnetic phase transitions such as collinear ferrimagnetism (FR) to noncollinear spin-flop transition in $Mn_2Mo_3O_8$ and AFM to FR transition in $Fe_2Mo_3O_8$ [1,2]. However, for practical applications, enhancement of their T_N or generation of spontaneous magnetization is demanded. Recently, epitaxial strain engineering has emerged as a powerful method for tuning the magnetism of oxide thin films. Although $M_2Mo_3O_8$ has not been prepared in thin film form so far, the epitaxial strain is expected to improve its magnetism. The purpose of the Ph.D. research is to investigate the magnetism of $Mn_2Mo_3O_8$ and $Fe_2Mo_3O_8$ thin films from both experimental and theoretical sides and to explore the possibility of realizing high-T_N $M_2Mo_3O_8$ materials.

2 Experimental and theoretical techniques

2.1 Pulsed laser deposition (PLD) method

The pulsed laser deposition (PLD) method is one of the physical vapor deposition techniques. Chemical composition, crystal structure, growth mode, and film quality are governed by various growth parameters conditions for the chamber, the substrate, the target, and laser (Table 2-1).

Table 2-1. The main growth parameters for the PLD method.

Parameters for	Parameter name
Substrate	Crystal structure
	Chemical composition
	Temperature
Chamber	Atmosphere gas
	Pressure
Laser	Frequency
	Energy
	Number of shots
Target	Chemical composition
	Density
	Surface flatness

The choice of the substrate is usually the most import because the structure of the surface of the substrate influences the structure of the film directory. For example, if one

wants to obtain a hexagonal-structure film, a substrate with hexagonal-structure surface including substrates will be chosen. As shown in the Section 1-3, the kind of strain, tensile or compression, is also an import factor of modification of the physical properties. In this study, I use the substrates which have larger in-plane lattice constants (e.g., Al_2O_3 (001), Yttria-stabilized zirconia (111) and $SrTiO_3$ (111)), aiming to shorten the out-of-plane lattice constant to enhance the weak out-of-plane magnetic interactions.

Figure 2-1(a) shows the appearance of the device. The PLD device can be mainly separated into two chambers, the load-lock chamber for the preparation and the main chamber for the fabrication. First, targets and substrates are all put into the main chamber and pumped out the air until the pressure is smaller than 10^{-6} Torr. Then open the valve between two chambers, transfer the samples into the main chamber and close the valve. After deposition, the samples are transferred into the load-lock chamber. This procedure makes sure that there is almost no contact between the atmosphere outside and that in the main chamber, which may cause the contamination.

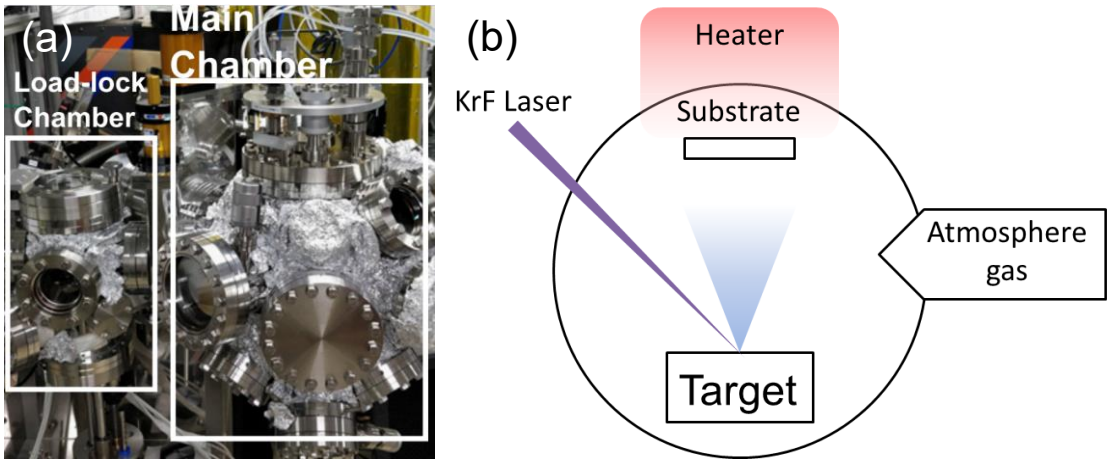

Figure 2-1. (a) The appearance of the PLD device. (b) A schematic view of the main chamber of the PLD device.

Figure 2-1(b) shows the schematic view of the main chamber. Inside a high

vacuum chamber with a base pressure of < 10^{-8} Torr, a pulsed laser (purple line) is irradiated onto a target, an oxide sintered body as a raw material. In my research, a KrF laser with a wavelength of 248 nm was used, and the target was made using a hot-press method. The plume (blue area), including the plasmatic state of the target, vertically heads to the substrate, which is heated by a heater (red area) at 400 ~ 1200 ℃, and the plume forms the thin film on the substrate. The temperature of the substrate during fabrication was measured by a pyrometer and controlled by lamp heating. Figure 2-2 shows the schematic illustration of the substrate holder. The substrates are fixed on a graphite board, and the lamp is heated from the backside. For improving the thermal contact between the graphite board and the substrates, Pt paste was used. In addition, during the deposition, gas (N_2, He, O_2, etc.) is introduced to the main chamber as a growth condition parameter

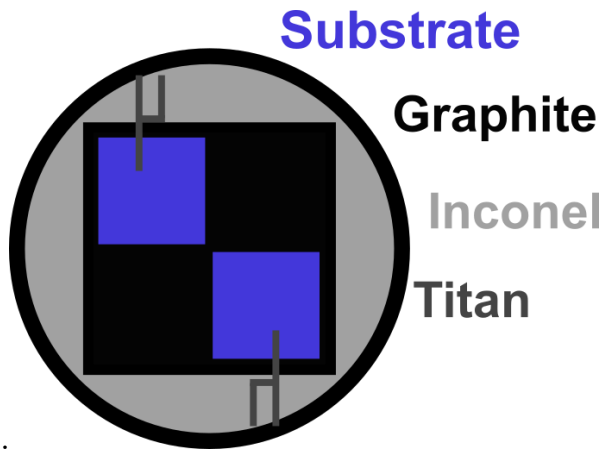

Figure 2-2. A schematic view of a substrate holder.

2.2 Thin film characterization

2.2.1 Crystal structure analysis by X-ray diffraction (XRD)

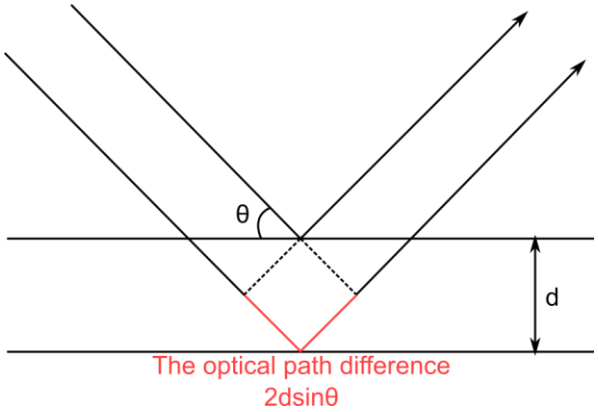

Figure 2-3. A schematic view of Bragg's law.

When an X-ray is irradiated into a crystal, the reflection will occur at crystal planes. As shown in Fig. 2-3, the reflected X-rays will cancel each other or strengthen each other with a certain angle of incidence. In the latter case, Bragg's law can be used to decide the distance between the crystal planes. Bragg's formula is as follow:

$$2d \sin\theta = n\lambda$$

where d is the distance between the crystal planes, θ is the angle of incidence, λ is the wavelength of incidental X-ray, and n is a possible integer. Bragg's formula means that an intense reflected X-ray would occur when the optical path difference is an integer multiple of the wavelength. While θ changes with λ are fixed, some intense reflected X-rays can be obtained when the equation holds to calculate d values.

In this study, XRD measurements were conducted with commercial four-axis diffractometers. 2θ for the X-ray detector, and ω, χ, and φ for the sample and the X-ray source (Fig. 2-4). Here, I mainly focus on the 2θ-θ measurement for determining the lattice constants and φ scan for finding relationships between the symmetry of the thin

films and the substrates.

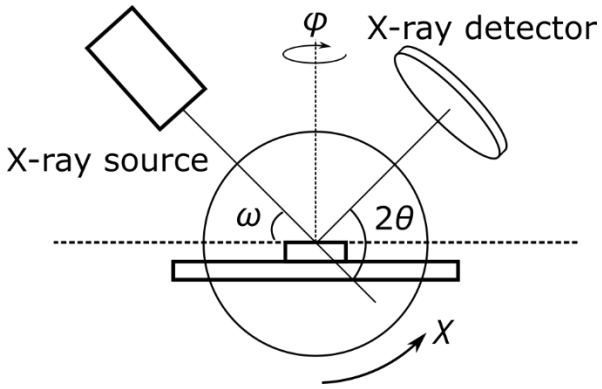

Figure 2-4. A schematic side view of a four-axis diffractometer.

2.2.2 Scanning transmission electron microscope (STEM)

Scanning transmission electron microscope (STEM) is a technique to obtaining the structure of a sample with atomic resolution by using a transmitted electron beam. To transmit the light through the sample, the shape of the sample prepared by a focused ion beam is usually a thin film with a thickness of ~ 100 nm. By detecting the transmitted electrons, several types of images can be obtained by different approaches. In this research, I focused on the annular dark-field (ADF) images. The significant advantage of the ADF image is the intensity of the signal (*I*) can be written in a functional of the atomic number, *Z*, as below [52]:

$$I \propto S^{-1} \sum_i Z_i^n$$

where *S* is the projected area of a unit cell, Z_i is the atomic number of the *i*th atom within the unit cell, and *n* is the parameter depending on the measurement setup. Therefore, STEM-ADF image is also called a *Z*-contrast technique.

Since the *Z*-contrast technique is a relative evaluation, it is difficult to obtain an absolute *Z* value of the atom. To account for this difficulty, energy dispersive X-ray

spectroscopy (EDX) is a strong option, and the EDX device is usually attached to a STEM platform. As EDS is named, an X-ray is used for EDS. While an X-ray focuses on a sample, an electron in an inner shell may be excited, ejected from the shell, and an electron-hole may occur. To get in this hole, a high-energy electron from the outer shell emits the energy in the form of an X-ray called characteristic X-ray. Since characteristic X-rays have specific energies depending on the element, elemental analysis can be performed by measuring these energies.

2.2.3 Atomic force microscope (AFM)

Atomic force microscope (AFM) is a type of microscope that detects the atomic force acting between a probe and a sample. The AFM probe is attached to the tip of a cantilever, and the probe is brought into contact with the surface of the sample by a small force. The surface profile is imaged by scanning the distance between the AFM probe and the sample horizontally while keeping the deflection of the cantilever a constant. The pressing force, a signal of the deflection of the cantilever, is detected by an optical lever system. A laser is irradiated on the back of the cantilever, and the reflected laser is detected by the position sensor with four sub sensors.

2.2.4 X-ray photoemission spectroscopy (XPS)

X-ray photoemission spectroscopy (XPS) is widely used as a technique not only for qualitative and quantitative analysis of elements existing in the material but also for a chemical bonding state analysis to determine the material's properties. Since XPS uses soft X-rays as the excitation source, slight damage to the sample is caused, and the charge of insulators can be easily removed. Therefore, XPS can be used to measure metallic materials and many other materials such as semiconductors, polymers, *etc*.

XPS spectra are obtained by irradiating the sample with an X-ray while measuring the energy of the escaping photoelectrons. The XPS spectra usually record the count of electrons as a function of the energy of the binding energy of electrons. Since the binding energy of the electrons in the same orbital will shift when the electrons' number changes, the valence state can be specified by comparing it with the spectra of a known compound.

2.2.5 X-ray absorption spectroscopy (XAS) and X-ray magnetic circular dichroism (XMCD)

Like XPS, XAS is the spectroscopy used to investigate the (local) electronic structure of the surface of the sample, and the X-ray beam is used. The measurement is usually performed at synchrotron radiation facilities because a tunable and intense X-ray source is needed. XAS spectra are obtained while tuning the photon energy and finding where the electrons can be excited.

X-ray magnetic circular dichroism (XMCD) is an application of XAS. A magnetic sample is irradiated with circularly polarized X-rays. The absorption spectrum differs depending on the sample's magnetization direction and the direction of the optical spin of the circularly polarized light. By conducting experiments using this phenomenon, it is possible to study magnetic materials, e.g., the magnetic orderings in my research.

2.2.6 Temperature-dependence and magnetic-field-dependence magnetic property characteristics

Magnetic property characteristics of the thin films were evaluated using Magnetic Property Measurement System (MPMS/MPMS®3) manufactured by Quantum Design. In this study, the magnetic moments (M) of $Mn_2Mo_3O_8$ and $Fe_2Mo_3O_8$ thin films depended on the temperature (T) and the magnetic field (H). The available ranges of T

and H are 1.8-400 K and ±7 T, respectively. The superconducting quantum interference device (SQUID) in an MPMS/MPMS3 is the magnetometer used to measure the slight change of M. The SQUID is based on superconducting loops containing Josephson junctions. An electric current flows through the loop when the magnitude of the magnetic flux changes. Detecting the voltage variation driven by the current enables magnetization measurement with high sensitivity.

2.3 Calculation method

Both the two topics in this thesis have two common calculation subjects: the crystal structure and the magnetism of the target material. For the optimization of the crystal structure, two approaches were used, (1) full structure optimization for initial structures from literature and (2) in-plane-lattice-constants-fixed structure optimization for estimating the strain effect from the substrate. All possible magnetic orderings were calculated during structure optimization to obtain the most stable one. In the first topic of $Mn_2Mo_3O_8$, all the calculation works were performed with a noncollinear setup in which the definition of the direction of the spin is not only up/down but a three-dimensional one, while a collinear setup was also used in the second topic of $Fe_2Mo_3O_8$ due to the limitations of the computing specs.

2.3.1 Band calculation based on the density functional theory

In this research, theoretical methods are used to investigate the mechanism of magnetism. First-principles calculation derives physical quantities (*e.g.*, total energy, lattice constant) by numerically solving a basic physical equation without using experimental results. Indeed, it is challenging to solve strictly in nearly infinite solids systems, and it is most likely to be deformed using various approximations. This section introduces several methods and approximation methods, mainly focusing on the density functional theory used in this research.

In order to obtain the physical quantity of the N-electron system, the Schrödinger equation of electrons is needed to be solved. However, even using several approximations such as Hartree approximation and Hartree-Fock approximation, it is difficult to solve the equation with $3N$ dimensions. Here, the calculation becomes possible by introducing DFT,

which deals with electrons as a density distribution. In this section, I will briefly introduce the derivation of DFT and the DFT+*U* method, an advanced method to make the result more accurate.

2.3.1.1 Hohenberg-Kohn theorems

Hohenberg-Kohn theorems [53] include the following two.

Theorem 1: *If the electron density* $n(\boldsymbol{r})$ *of the ground state is determined, the external field* $v_{ext}(\boldsymbol{r})$ *potential and the wavefunction* $|\Psi\rangle$ *will be determined in one way.*

Theorem 2: *There is an energy functional with* $v_{ext}(\boldsymbol{r})$ *as a parameter, and it takes the minimum value when giving* $n(\boldsymbol{r})$ *of the ground state.*

From these theorems, the wave functions derived from the Schrödinger equation the energy functional of the ground state can be defined as follows,

$$E_v[n] = F[n] + \int n(\boldsymbol{r}) v_{ext}(\boldsymbol{r}) d\boldsymbol{r}$$

where $F[n]$ is defined as Hohenberg-Kohn functional and can be written as follows,

$$F[n] = \langle \Psi | T + V_{ee} | \Psi \rangle$$

where T is the kinetic energy of the electron and V_{ee} is the electron-electron interaction which can separate into classic action and quantum effect as follows:

$$V_{ee}[n] = \frac{1}{2} \int n(\boldsymbol{r}) V_{\mathrm{H}}(\boldsymbol{r})\, d\boldsymbol{r} + E_{\mathrm{xc}}[n],$$

$$V_{\mathrm{H}}(\boldsymbol{r}) = \int \frac{n(\boldsymbol{r}')}{|\boldsymbol{r} - \boldsymbol{r}'|} d\boldsymbol{r}'$$

$E_{\mathrm{xc}}[n]$ is the term from the exchange-correlation. By using Hohenberg-Kohn theorems, the new electron density $n'(\boldsymbol{r})$ can be determined as $n \Rightarrow v \Rightarrow n'$. Comparing n and n', if they are equal, which is called converged, it means a ground state of electron density is

obtained. This process is called a self-consistent field (SCF).

2.3.1.2 Kohn-Sham equation

In order to obtain $F[n]$, the Kohn-Sham orbital $\varphi(\boldsymbol{r})$, which is also called the wave function is introduced. In the case of the N-electron system, $n(\boldsymbol{r})$ and $T[n]$ can be represented as follows, respectively:

$$n(\boldsymbol{r}) = \sum_{i}^{N} |\varphi_i(\boldsymbol{r})|^2 \, , T[n] = -\frac{1}{2}\sum_{i}^{N} \langle \varphi_i | \nabla^2 \varphi_i \rangle$$

Combining $E_{\mathrm{xc}}[n]$ and the difference between $T[n]$ and true kinetic energy, exchange-correlation potential, which is also named exchange-correlation functional, of the electron can be defined as follow:

$$v_{\mathrm{xc}}[n(\boldsymbol{r})] \equiv \frac{\delta E_{\mathrm{xc}}[n(\boldsymbol{r})]}{\delta n(\boldsymbol{r})}$$

As a result, total energy can be represented as follow:

$$E_{\mathrm{DFT}} = \sum_{i}^{N} \varepsilon_i - \frac{1}{2}\int n(\boldsymbol{r}) V_{\mathrm{H}}(\boldsymbol{r}) d\boldsymbol{r} + E_{\mathrm{xc}}[n(\boldsymbol{r})] - \int n(\boldsymbol{r}) v_{\mathrm{xc}}[n(\boldsymbol{r})] \, d\boldsymbol{r},$$

which is called the Kohn-Sham equation, and ε_i is the energy of the Kohn-Sham orbital. The second term is the correction of double-counted electron-electron Coulomb interaction. The third and fourth terms are called exchange-correlation energy (E_{XC}).

2.3.1.3 Exchange-correlational functionals (E_{XC})

The existence of the $v_{\mathrm{XC}}[n(\boldsymbol{r})]$ is guaranteed by the first theorem of the Hohenberg-Kohn theorems. However, since the exact form of E_{XC} or $v_{\mathrm{XC}}[n(\boldsymbol{r})]$ is unknown, E_{DFT} still cannot be calculated. Therefore, an approximated form of E_{XC} is used widely during the calculation.

2.3.1.4 Local density approximation (LDA)

Local density approximation (LDA) [54] is the simplest approximated form, which is based on applying a potential of the homogeneous electron gas to the system. The form of E_{XC} is defined as

$$E_{\mathrm{xc}}\big(n(\boldsymbol{r})\big) \equiv \int n(\boldsymbol{r})\varepsilon_{\mathrm{xc}}\big(n(\boldsymbol{r})\big)d\boldsymbol{r}.$$

Note that E_{XC} is no longer functional but the function of $n(\boldsymbol{r})$. While LDA works well for metals, it results in a significant error in an insulator or semiconductor system because of the non-homogeneity of the real system.

2.3.1.5 Generalized gradient approximation (GGA)

Generalized gradient approximation (GGA) [55] is one of the approaches to exceed LDA. While LDA assumes that electron density is the same everywhere, GGA introduces the gradient effect $\delta n(\boldsymbol{r})$. One by Perdew, Burke, and Ernzerhof (PBE) [56] is most widely used among several implementation types. However, even PBE cannot reasonably estimate the transition-metal insulator system, underestimating the bandgap.

2.3.1.6 LDA(GGA) + *U* method

Since LDA(GGA) employs the mean-field approximation of the uniform electron gas, the effect of electron density fluctuation is neglected. Therefore, the LDA(GGA) + *U* method clarifies the electron Coulomb repulsion and the contribution from the exchange interaction. First, I show the energy functional that tackled the Hubbard term as follow,

$$E_{\mathrm{LDA}+U}[n(\boldsymbol{r})] = E_{\mathrm{LDA}}[n(\boldsymbol{r})] + E_{\mathrm{Hub}}[\{n_{mm\prime}^{I\sigma}\}] - E_{\mathrm{DC}}[\{n_{m}^{I\sigma}\}]$$

where $n_m^{I\sigma}$ is the electron density of site *I*. $E_{\mathrm{DC}}[\{n_m^{I\sigma}\}]$ is the term to cancel the double

count of the first and the second terms, which often takes the sum of the electron density of the whole system. They can be represented as follows:

$$E_{\mathrm{Hub}}\left[\{n^{I}_{mm'}\}\right] = \frac{1}{2}\sum_{\{m\},\sigma,I}\{\langle m,m''|V_{ee}|m',m'''\rangle n^{I\sigma}_{mm'}n^{I-\sigma}_{m''m'''} + (\langle m,m''|V_{ee}|m',m'''\rangle - \langle m,m''|V_{ee}|m''',m'\rangle)n^{I\sigma}_{mm'}n^{I\sigma}_{m'''}\}$$

$$E_{\mathrm{DC}}[\{n^{I}\}] = \sum_{I}\frac{U}{2}n^{I}(n^{I}-1) - \sum_{I}\frac{J}{2}\left[n^{I\uparrow}\left(n^{I\uparrow}-1\right) + n^{I\downarrow}\left(n^{I\downarrow}-1\right)\right]$$

Simplification can be made between these two terms as a correction term as follow:

$$E_{U}[n^{I\sigma}_{mm'}] = E_{\mathrm{Hub}}[\{n^{I\sigma}_{mm'}\}] - E_{\mathrm{DC}}[\{n^{I}\}] = \frac{U}{2}\sum_{I,\sigma}\sum_{i}\lambda^{I\sigma}_{i}(1-\lambda^{I\sigma}_{i})$$

To make $E_{\mathrm{LDA}+U}$ minimum, full occupation ($\lambda^{I\sigma}_{i} = 1$) or complete empty ($\lambda^{I\sigma}_{i} = 0$) of the orbital works better. In fact, according to Janak's theorem [56], the total energy of the system can be represented as:

$$E_{n} = (1-\omega)E_{N} + \omega E_{N+1}$$

which means the change in total energy should be a polygonal line, as shown in Fig. 2-5. Since the LDA (black line) cannot reproduce Janak's theorem well, *U* (blue line) works as a corrective term, which makes DFT more accurate.

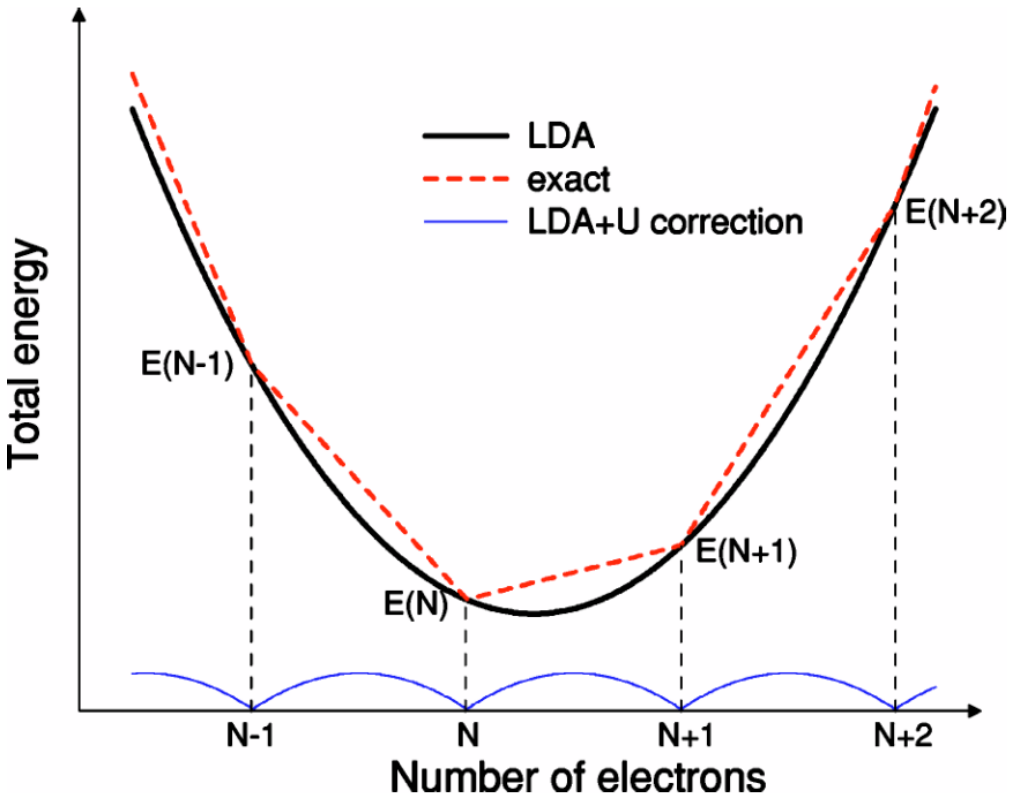

Figure 2-5. Schematic image of the total energy of an isolated atomic system in contact with an electron reservoir. The black and red lines depict results with the LDA and the exact formulation, respectively. The blue line is the difference between them to be corrected by the LDA/GGA + *U* method. Reprinted with permission from Ref. [57]. Copyright 2005 by the American Physical Society.

2.3.2 Diabatic approximation and first-principles molecular dynamics method

The discussion so far has been based on the assumption that the position of the ions (atoms) is fixed, and that the energy of the electrons is sufficiently more significant than the kinetic energy, even when there are actual thermal oscillations. So, the electronic state doesn't depend on the ion velocity. This approximation is called diabatic approximation or Born-Oppenheimer approximation [58]. With this approximation, the total energy of the system is the energy functional of DFT with the addition of classic kinetic energy as follow:

$$E = \frac{1}{2}\sum_{n} M_n \left|\dot{\boldsymbol{R}}_n\right|^2 + E_{DFT}[\{\boldsymbol{R}_n\},\{\varphi_{i\sigma}\}]$$

To obtain the most stable structure, the minimum of E, the first-principles molecular dynamics method, which is also named the Car-Parrinello method, was developed. First, the Lagrangian is defined as:

$$\mathcal{L} = \frac{1}{2}\sum_{n} M_n \left|\dot{\boldsymbol{R}}_n\right|^2 + \sum_{i\sigma}\int d\boldsymbol{r}\mu_e|\dot{\varphi_{i\sigma}}(\boldsymbol{r})|^2 - E_{\mathrm{DFT}}[\{\boldsymbol{R}_n\},\{\varphi_{i\sigma}\}] + \sum_{ij\sigma}\Lambda_{ij\sigma}\left(\int d\boldsymbol{r}\varphi^*_{i\sigma}(\boldsymbol{r})\varphi_{j\sigma}(\boldsymbol{r}) - \delta_{i,j}\right)$$

for $\{\boldsymbol{R}_n\}$ and $\{\varphi_{i\sigma}\}$, where μ_e is the virtual mass and Λ_{ijk} is the undetermined coefficient of Lagrangian. $\varphi_{i\sigma}$ can be treated as generalized coordinates, and the equations of motion can be expressed as

$$M_n\ddot{\boldsymbol{R}}_n = -\nabla_{\boldsymbol{R}(\mathrm{n})}E_{\mathrm{DFT}}$$

$$\mu_e\ddot{\varphi}_{i\sigma}(\boldsymbol{r}) = -\frac{\delta E_{\mathrm{DFT}}}{\delta\varphi^*_{i\sigma}(\boldsymbol{r})} + \sum_{\sigma}\Lambda_{ij\sigma} = -\left(-\frac{\hbar^2}{2m}\nabla^2 + v^{\sigma}_{\mathrm{eff}}(\boldsymbol{r})\right)\varphi_{i\sigma}(\boldsymbol{r}) + \sum_{\sigma}\Lambda_{ij\sigma},$$

which shows there is no necessity to determine the eigenstate of the electronic state (diagonalize the matrix). During calculating, there are many ways to accelerate

convergence. For example, in many cases, first-order differential equations are used instead of second-order derivatives (steepest descent method, conjugate gradient method) as shown following:

$$\mu_e' \dot{\varphi}_{i\sigma}(\boldsymbol{r}) = -\frac{\delta E_{\mathrm{DFT}}}{\delta \varphi_{i\sigma}^*(\boldsymbol{r})} + \sum_{\sigma} \Lambda_{ij\sigma}$$

where μ_e' is appropriately chosen to obtain $\dot{\varphi}_{i\sigma}(\boldsymbol{r}) = 0$.

Next, about the displacement of ions, the force for moving the ions can be written as

$$\begin{aligned}
\boldsymbol{F}_n &= -\boldsymbol{\nabla}_{\boldsymbol{R}_n} \left\{ E_{\mathrm{DFT}} + \sum_{ij\sigma} \Lambda_{ij\sigma} \int d\boldsymbol{r} \varphi_{i\sigma}^*(\boldsymbol{r}) \varphi_{j\sigma}(\boldsymbol{r}) \right\} \\
&= -\boldsymbol{\nabla}_{\boldsymbol{R}_n} E_{\mathrm{DFT}}^{\mathrm{ion-ion}} - \boldsymbol{\nabla}_{\boldsymbol{R}_n} \left(E_{\mathrm{DFT}}^{\mathrm{electron}} - \sum_{ij\sigma} \Lambda_{ij\sigma} \int d\boldsymbol{r} \varphi_{i\sigma}^*(\boldsymbol{r}) \varphi_{j\sigma}(\boldsymbol{r}) \right) \\
&= \boldsymbol{F}_n^{\mathrm{ion}} + \boldsymbol{F}_n^{\mathrm{electron}}.
\end{aligned}$$

The first and second terms are forces for ion-ion interaction and electron-electron interaction, respectively. By using the Hellmann-Feynman theorem, $\boldsymbol{F}_n^{\mathrm{electron}}$ can be represented as

$$\begin{aligned}
\boldsymbol{F}_n^{\mathrm{electron}} &= -\boldsymbol{\nabla}_{\boldsymbol{R}_n} \left(E_{\mathrm{DFT}}^{\mathrm{electron}} - \sum_{ij\sigma} \Lambda_{ij\sigma} \int d\boldsymbol{r} \varphi_{i\sigma}^*(\boldsymbol{r}) \varphi_{j\sigma}(\boldsymbol{r}) \right) \\
&= -\boldsymbol{\nabla}_{\boldsymbol{R}_n} \left(E_{\mathrm{DFT}}^{\mathrm{e-e}}[\{\boldsymbol{R}_n\}, n] + \int d\boldsymbol{r}\, n(\boldsymbol{r}) V_{\mathrm{ion}}^n(\boldsymbol{r} - \boldsymbol{R}_n) \right. \\
&\qquad \left. - \sum_{ij\sigma} \Lambda_{ij\sigma} \int d\boldsymbol{r} \varphi_{i\sigma}^*(\boldsymbol{r}) \varphi_{j\sigma}(\boldsymbol{r}) \right) \\
&= -\int d\boldsymbol{r}\, n(\boldsymbol{r}) \boldsymbol{\nabla}_{\boldsymbol{R}_n} V_{\mathrm{ion}}^n(\boldsymbol{r} - \boldsymbol{R}_n) - \int d\boldsymbol{r}\, V_{\mathrm{ion}}^n(\boldsymbol{r} - \boldsymbol{R}_n) \boldsymbol{\nabla}_{\boldsymbol{R}_n} n(\boldsymbol{r}) + \boldsymbol{F}_n'
\end{aligned}$$

and the first term on the right side doesn't depend on the change of electron density.

Combining with $\boldsymbol{F}_n^{\mathrm{ion}}$, Hellmann-Feynman force [59] is defined as

$$\boldsymbol{F}_n^{\mathrm{HF}} \equiv \boldsymbol{F}_n^{\mathrm{ion}} - \int d\boldsymbol{r}\, n(\boldsymbol{r}) \boldsymbol{\nabla}_{\boldsymbol{R}_n} V_{\mathrm{ion}}^n(\boldsymbol{r} - \boldsymbol{R}_n).$$

In addition, the remaining $\boldsymbol{F}_n'$ is called the variational force or Pulay force. This term will be zero when it satisfies the Kohn-Sham equation and the standard orthogonality condition. In other words, approximations used in DFT make this term not to be zero, which makes it necessary to estimate the magnitude of the Pulay force. Structure optimization is terminated if these values are below the threshold.

The flow up to here is as shown in Fig. 2-6.

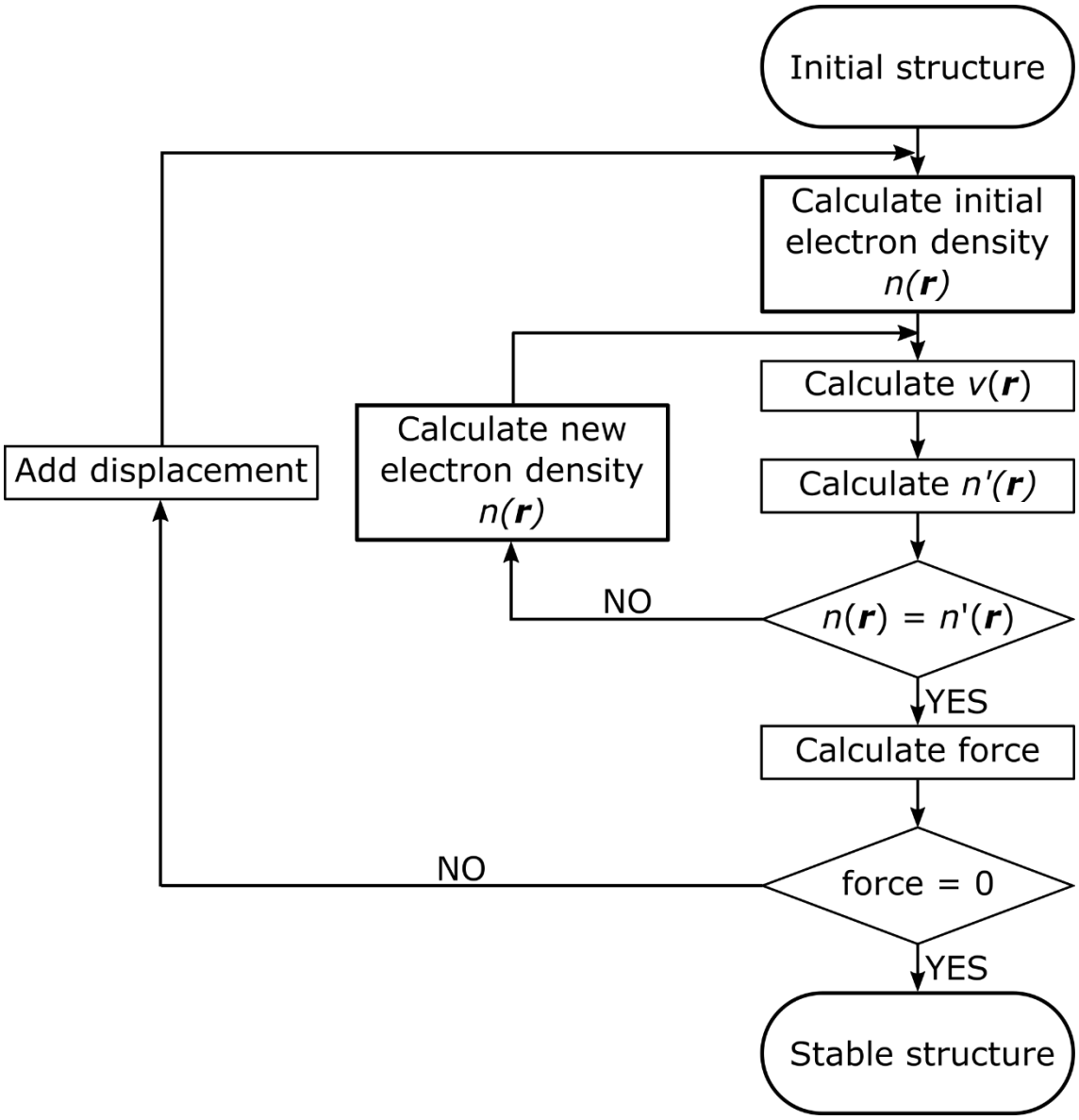

Figure 2-6. A chart of structure optimization.

2.3.3 Optimization of the magnetic ordering

In this thesis, the decision of the most table magnetic ordering is based on DFT calculation. In an *n*-atom collinear spin system, all the magnetic atoms have an up spin or a down spin. The number of the magnetic orderings (combinations of the spins) is 2^{n-1}. Different from the optimization of the crystal structure, the stabilization energy of a specific magnetic ordering is usually slight. Starting from a specific magnetic ordering

which is event not a most stable one, the output magnetic ordering keeps the same in most cases. This means the SCF cannot optimize the magnetic ordering, and the comparison of the total energies is needed. Then, I calculated the total energies with all possibilities of the magnetic orderings and the most stable magnetic ordering is the one with the lowest total energy.

2.3.4 The determination of the magnetic interaction coefficients

In order to compare the magnetic interaction among several materials, I calculate the coefficients of magnetic exchange interaction (J), DM interaction ($\boldsymbol{D}$), and single-ion anisotropy (SIA; Δ).

2.3.4.1 Magnetic exchange interaction

The magnetic exchange interaction is evaluated using the Heisenberg model:

$$E = E_0 + \frac{1}{2}\sum_P J_P \sum_{(i,j)\in P} S_i S_j$$

where S is the magnetic moment of magnetic ions, J is the coupling energy between a pair of S, and P denotes a group of symmetrically identical pairs (i, j) to distinguish J. The intercept E_0 corresponds to the energy without the magnetic interaction. Here, we define a positive J as an antiferromagnetic coupling between two spins while a negative J represents ferromagnetic coupling. In this study, I estimated the magnetic coupling energy J (and the intercept E_0) by performing a multiple regression analysis. First, I calculate total energies for all possibilities of magnetic orders and performed linear regression to the Heisenberg model.

2.3.4.2 Dzyaloshinskii-Moriya interaction and single-ion anisotropy

With a noncollinear spin configuration, DM interaction and SIA are introduced, and the total energy can be represented as:

$$E = E_{\text{nonmag}} + E_J + E_{DM} + E_{SIA}$$
$$= E_{\text{nonmag}} + \frac{1}{2}\sum_P \left(J_P \sum_{(i,j)\in P} S_i \cdot S_j + \boldsymbol{D}_P \cdot \left(\sum_{(i,j)\in P} S_i \times S_j \right) \right) + \sum_n \Delta_n (\boldsymbol{S}_n^Z)^2.$$

In this model, $\boldsymbol{D}$ is vector and according to Moriya's rules, there is only one direction for $\boldsymbol{D}$ in $M_2Mo_3O_8$ which can be also represented as a vector (0, *D*, 0). In order to calculate the $\boldsymbol{D}$ value between the nearest-neighbor M^{2+} pair and Δ for *tetra*-/*octa*-M^{2+}, I calculate the total energies of four magnetic orderings and determine the *D* and Δ as shown in Fig. 2-7 and Fig. 2-8.

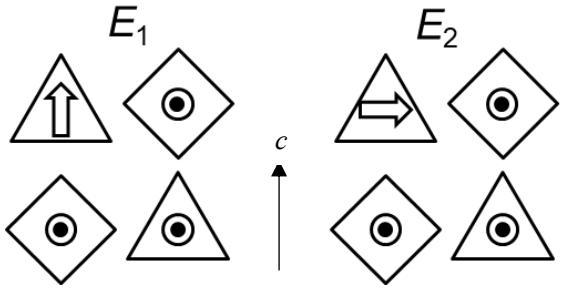

$$E_1 = \Delta S_Z^2 + E_{\text{other}}$$
$$E_2 = E_{\text{other}}$$
$$\Delta = \frac{E_1 - E_2}{S_Z^2}$$

Figure 2-7. The determination of the coefficient of SIA of *tetra*-M^{2+}. Triangles/squares represent *tetra*-/*octa*-M^{2+} ions. The arrows represent the directions of the spins. E_{other} is the term which is not related to SIA.

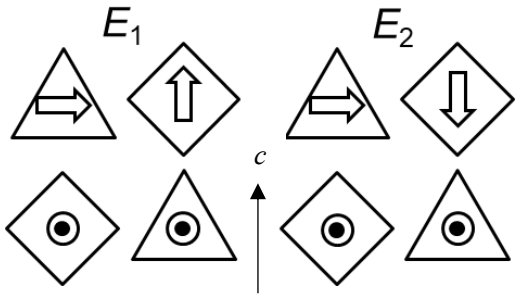

$$E_1 = -DS_Z^2 + \Delta S_Z^2 + E_{\text{other}}$$
$$E_2 = DS_Z^2 + \Delta S_Z^2 + E_{\text{other}}$$
$$D = \frac{E_2 - E_1}{2S_Z^2}$$

Figure 2-8. The determination of the *D* value bewteen *octa*- and *tetra*-M^{2+}. Triangles/squares represent *tetra*-/*octa*-M^{2+} ions. The arrows represent the directions of the spins. E_{other} is the term which is not related to DM interaction beween the nearest-neighbor M^{2+} pairs.

3 Epitaxial strain-induced large spontaneous magnetization in $Mn_2Mo_3O_8$ thin films*

3.1 Introduction

Multiferroic materials characterized by both ferroelectric and magnetic orders have been extensively studied because of their novel applications, such as fast-writing and low-energy-consumption nonvolatile data storage. [12,60] $M_2Mo_3O_8$ (M = Mn, Fe, Co, and Ni) is a promising multiferroic material exhibiting unique properties such as magnetic-(electric-)field-induced modulation of polarization (magnetization), giant thermal Hall effect, and a large variety of magnetism. [2,26,31,60] $M_2Mo_3O_8$ consists of tetrahedral (*tetra*-) and octahedral (*octa*-) M sites and Mo trimers (Fig. 3-1(a)) and has ferroelectric polarization along the *c*-axis. As for $Mn_2Mo_3O_8$, it possesses a ferrimagnetic (FR) spin order, in which the magnetic moments of Mn^{2+} ($3d^5$) align collinearly along the *c*-axis with antiferromagnetic interactions between *tetra*- and *octa*-Mn (Fig. 3-1(b)). The magnetic moments of *tetra*-Mn^{2+} and *octa*-Mn^{2+} almost cancel each other, and thus, the remanent magnetization determined from M-H measurements (M_r) is very low (0.01 μ_B/f.u. at 2 K) [2]. By applying an external magnetic field (H), the collinear FR phase switches to a non-collinear spin flop (SF) phase [2]. In the SF phase (Fig. 3-1(c)), the magnetic moments of *tetra*-Mn^{2+} and *octa*-Mn^{2+} are canted from each other, resulting in

* This chapter contains the contents of the following publication.

"Epitaxial-Strain-Induced Spontaneous Magnetization in Polar $Mn_2Mo_3O_8$"
Shishin Mo, Tsukasa Katayama, Akira Chikamatsu, Miho Kitamura, Koji Horiba, Hiroshi Kumigashira, and Tetsuya Hasegawa, Chem. Mater. **33**, 7713 (2021).

more significant magnetization than that of the FR phase [2]. Thus, stabilization of a non-collinear spin order might lead to an enlarged spontaneous magnetization, which is required for practical applications.

Recently, epitaxial strain engineering has emerged as a powerful method for tuning the magnetism of oxide thin films. For example, the non-collinear cycloidal spin order in $BiFeO_3$ changes to a canted G-type antiferromagnetic order by applying tensile or compressive strains less than 0.5% or greater than −1.6%, respectively, resulting in spontaneous magnetization [61]. In $LaCoO_3$, a low-spin state to a mixed intermediate-/high-spin state transition is induced by an approximate tensile strain of 1% [42]. The easy axis of $LaCoO_3$ films can be switched between in-plane and out-of-plane directions by using the strain [43]. Herein, I report the synthesis and magnetism of *c*-axis oriented $Mn_2Mo_3O_8$ epitaxial films grown on an Al_2O_3(001) substrate using 0.5% tensile strain. X-ray photoemission spectroscopy (XPS) and X-ray absorption spectroscopy (XAS) measurements revealed that Mn and Mo ions exist mainly as divalent and tetravalent ions, respectively. The $Mn_2Mo_3O_8$ films exhibited a magnetic order with a much larger M_r (0.35 μ_B/f.u.) than in case of bulk (0.01 μ_B/f.u.) [2] at 2 K, suggesting that a non-collinear spin structure, with magnetic moments tilted from the *c*-axis, is induced by the epitaxial tensile strain. The remanent magnetization was directed in the in-plane direction, which is in contrast to that of bulk $Mn_2Mo_3O_8$, which has a magnetic easy axis along the *c*-axis, supporting the above-mentioned non-collinear spin scenario.

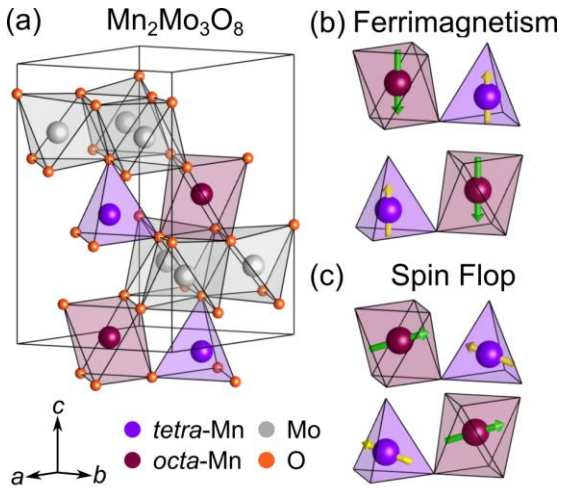

Figure 3-1. (a) Crystal structure of hexagonal $Mn_2Mo_3O_8$ and spin orders in (b) ferrimagnetic (FR) and (c) spin flop (SF) phases.

3.2 Experiments

$Mn_2Mo_3O_8$ thin films were fabricated on Al_2O_3(001) substrates using pulsed laser deposition (PLD). The PLD target was prepared by annealing a mixture of MnO, Mo, and MoO_3 (molar ratio of MnO:Mo:MoO_3 = 2:1:2) powders at 900 °C using a hot-press method. PLD deposition was conducted at 850 °C in Ar/H_2 (97:3) gas at a pressure of 10^{-4} Torr. After deposition, a 2-nm-thick Al_2O_3 capping layer was further deposited using PLD at room temperature and a background pressure of ~10^{-7} Torr. The resulting films had thicknesses of ~140 nm.

The crystal structures were evaluated using high-resolution X-ray diffraction (XRD) using Cu-$K\alpha_1$ radiation (Bruker, D8 DISCOVER). The valence states of the Mo ions were evaluated using Mo 3*d* XPS. The binding energy was determined relative to the Fermi edge of a gold foil in electrical contact with the samples. The valence states of Mn ions were determined using XAS near the Mn $L_{2,3}$-edge using the total-electron-yield method. The XPS and XAS measurements were conducted at beamline 2A of the Photon

Factory, KEK. Scanning transmission electron microscopy (STEM) measurements were performed with a JEOL ARM200F. The magnetization of the films was measured using a superconducting quantum interference device (SQUID) magnetometer (Quantum Design MPMS XL).

Band calculations based on density functional theory (DFT) were performed using the Vienna ab initio simulation package [62–65]. The Perdew–Burke–Ernzerhof generalized gradient approximation (PBE) was used for the exchange-correlation function [66]. The localized nature of the *d* electrons in Mn and Mo was treated using the PBE+*U* method with *U* values of 3.9 and 4.38 eV for Mn and Mo, respectively [67]. The valence states, including $3p^6 3d^6 4s^1$ of Mn, $4s^2 4p^6 4d^5 5s^1$ of Mo, and $2s^2 2p^4$ of O, were described on a plane-wave basis with a cutoff energy of 700 eV. The other core electrons were considered by employing the projector augmented wave method [68,69]. Brillouin zone integration was performed using a Γ-centered 3 × 3 × 2 **k**-point mesh for structure optimization and a Γ-centered 5 × 5 × 3 **k**-point mesh for electronic structure calculation. The ionic positions and lattice constants of bulk $Mn_2Mo_3O_8$ were optimized for FR-$Mn_2Mo_3O_8$ with spin-orbital coupling included such that the residual force on an atom and the pressure on the cell was smaller than 0.01 eV $Å^{-1}$ and 0.1 GPa, respectively. In addition, the *c*-axis length of film $Mn_2Mo_3O_8$ was recalculated by fixing the in-plane lattice constants with a strain between +0.5% and +3.0%. The crystal structures were visualized using VESTA [28].

3.3 Results and discussion

3.3.1 Structural characterization

Figure 3-2(a) shows the out-of-plane $2\theta-\theta$ XRD pattern of the fabricated $Mn_2Mo_3O_8$ film on the Al_2O_3(001) substrate. The film exhibited $Mn_2Mo_3O_8$ *002*, *004*, *006*, *008*, and *00<u>10</u>* diffraction peaks without any impurity peaks, indicating the successful formation of the *c*-axis oriented $Mn_2Mo_3O_8$ film. In order to investigate the in-plane relation between the film and the substrate, ϕ-scan measurements were performed around the $Mn_2Mo_3O_8$ {112} and Al_2O_3 {116} diffraction peaks (Fig. 3-2(b)). The film {112} peaks appeared every 60°, confirming hexagonal symmetry around the film normal. The ϕ values of the {112} film peaks were shifted by 30° from those of the Al_2O_3 {116} peaks. These results imply that the [100] and [001] directions of the $Mn_2Mo_3O_8$ film are parallel to the [120] and [001] directions of the Al_2O_3 substrate, respectively. In these orientations, Mo_6 hexagons in the film and Al_6 hexagons in the substrate can have a similar orientation relation as illustrated in Fig. 3-3. When considering the in-plane relations, compressive strain is expected because the distance between the Mo_6 hexagons in the film ($\sqrt{3} \times a$ of $Mn_2Mo_3O_8$ = 10.0 Å: Fig. 3-3(a)) is 5.7 % longer than the corresponding distance in the substrate ($2 \times a$ of Al_2O_3 = 9.5 Å: Fig. 3-3(b)). However, the lengths of *a*- and *c*-axes evaluated from the *00k* and *112* diffraction peaks, 5.83 Å and 10.17 Å, respectively, are 0.5% longer and 1.0% shorter than those of bulk $Mn_2Mo_3O_8$ (a_{bulk} = 5.8003 Å and c_{bulk} = 10.2425 Å) [70], indicating that the films undergo a sizeable tensile strain from the Al_2O_3 substrate. I speculate that higher-order matching takes place; for example, $8 \times a$ of the $Mn_2Mo_3O_8$ film (46.40 Å) has good matching with $(17/\sqrt{3}) \times a$ of Al_2O_3 (46.72 Å) with a mismatch of 0.7% (Fig. 3-4). Such higher-order lattice matching is also observed in ZnO films on Al_2O_3 (001) substrates and Fe_3O_4 films on

$SrTiO_3$ (001) substrates [71,72].

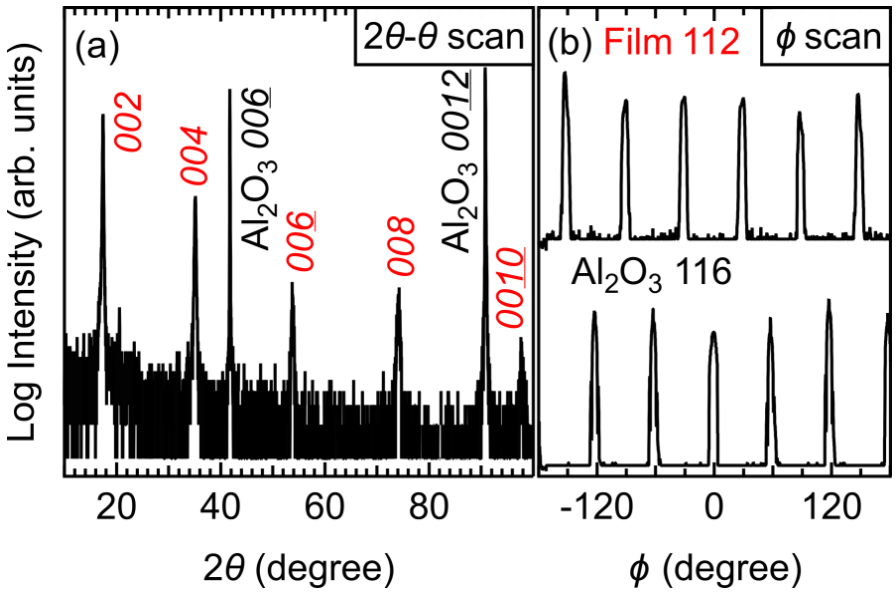

Figure 3-2. (a) Out-of-plane 2θ–θ XRD pattern and (b) ϕ-scan of the $Mn_2Mo_3O_8$ film on the Al_2O_3 substrate.

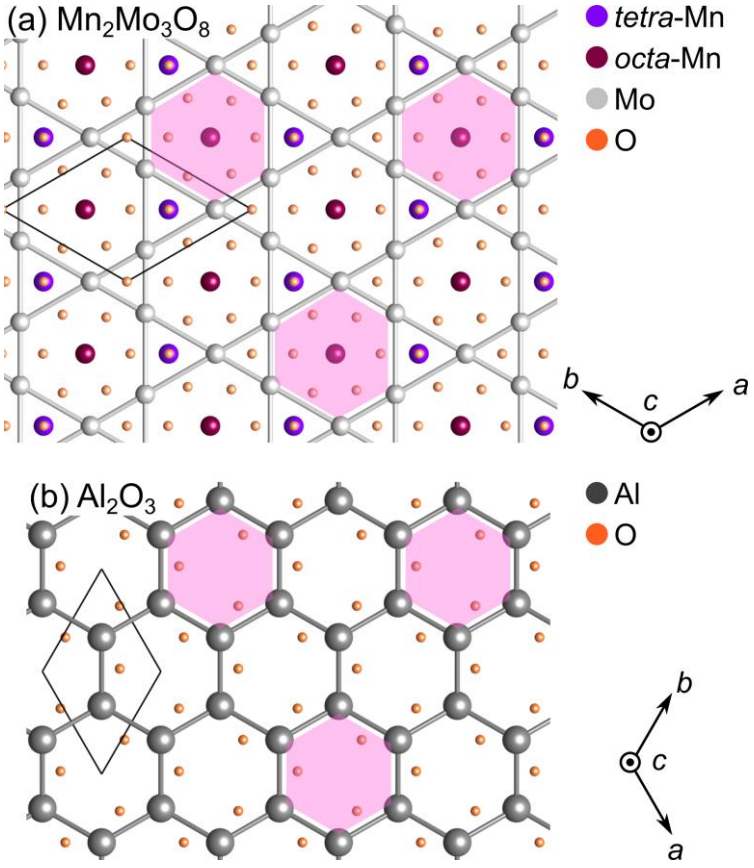

Figure 3-3. Top-view ionic arrangements of the crystal structures of (a) $Mn_2Mo_3O_8$ and (b) Al_2O_3. Pink hexagons in Figs. (a) and (b) show Mo_6 hexagons and Al_6 hexagons, respectively.

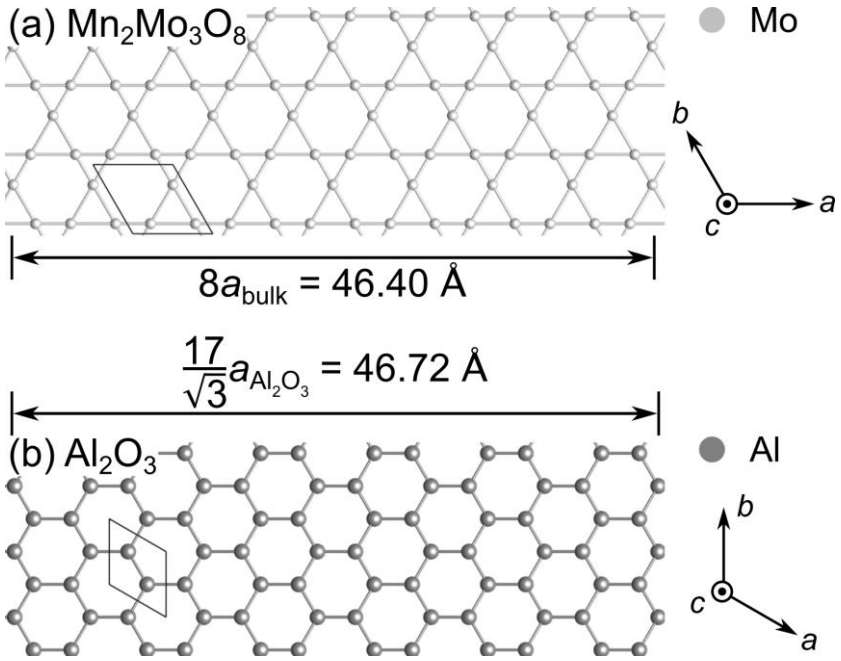

Figure 3-4. Top-view cationic arrangements of the crystal structures of (a) $Mn_2Mo_3O_8$ film (Mn ions are omitted for clarity) and (d) Al_2O_3 substrate.

I evaluated the valence states of Mo and Mn ions in the $Mn_2Mo_3O_8$ film using XPS and XAS measurements. Figure 3-5(a) shows the Mo 3*d* spectrum of the film. The spectrum has two main peaks at 231.6 and 234.7 eV, which correspond to $3d_{5/2}$ and $3d_{3/2}$ for the Mo^{4+} component, respectively, with small Mo^{3+} and Mo^{5+} components [73]. The spectral weights of Mo^{5+}:Mo^{4+}:Mo^{3+} were 12:76:12, and thus, it can be concluded that the Mo ions exist mainly as tetravalent in the film. Figure 3-5(b) shows the Mn $L_{2,3}$ XAS spectrum of the $Mn_2Mo_3O_8$ film and the spectra of $SrMnO_3$, $LaMnO_3$, $YBaMn_3AlO_7$, and MnO as references for Mn^{4+}, Mn^{3+}, *tetra*-Mn^{2+}, and *octa*-Mn^{2+}, respectively [74,75]. The main Mn L_3 edge peak of the $Mn_2Mo_3O_8$ film was located at 640.8 eV, with three shoulder peaks at 639.8, 642.2, and 644.5 eV. From the shape and position of the peaks, the valence states of Mn were determined to be divalent at the *tetra*- as well as *octa*-Mn sites. Consequently, the $Mn_2Mo_3O_8$ film consists of Mo^{4+} and Mn^{2+} ions, similar to that in the case of bulk $Mn_2Mo_3O_8$ [2].

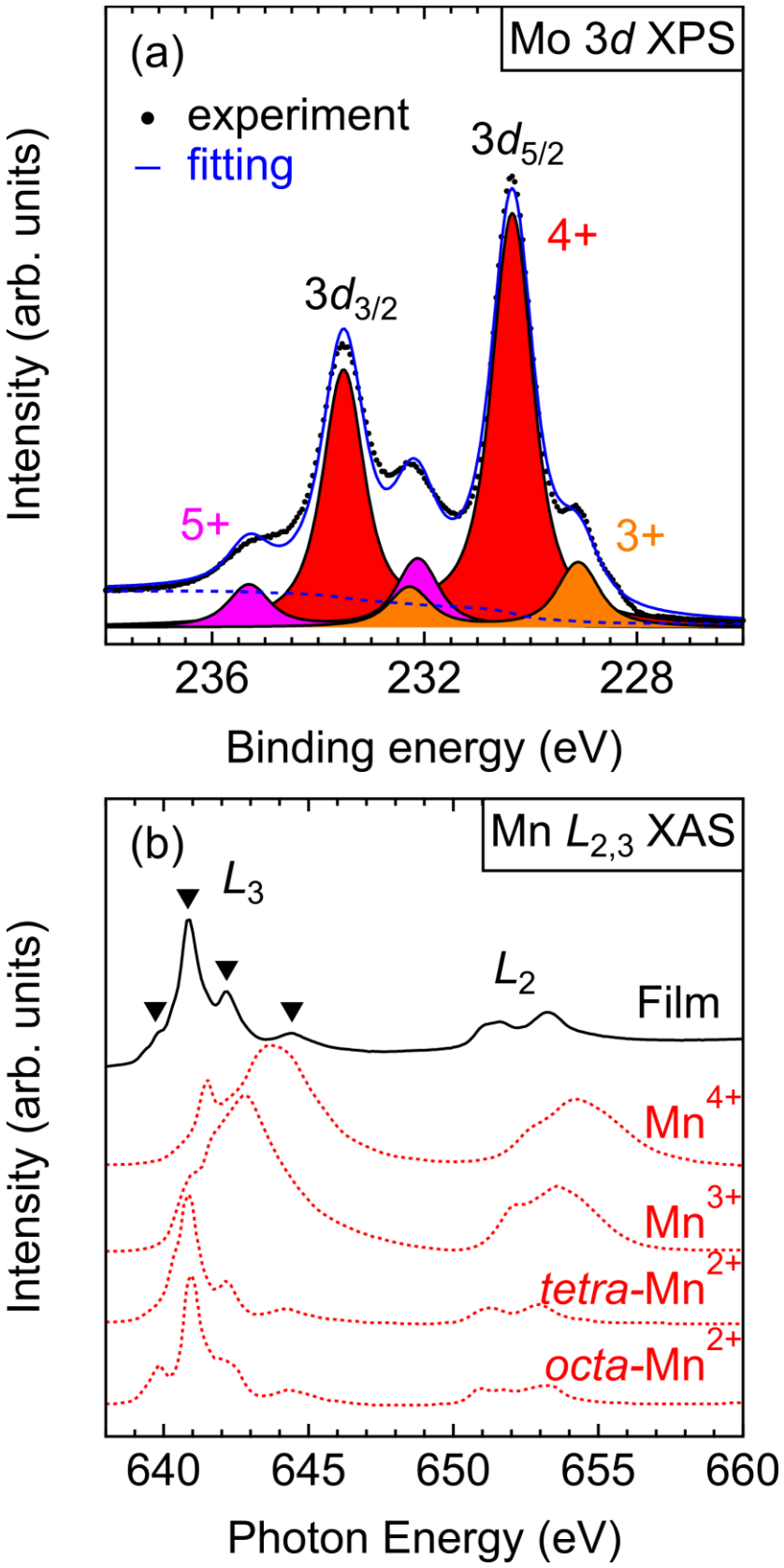

Figure 3-5. (a) Mo 3*d* XPS and (b) Mn $L_{2,3}$ XAS spectra for a $Mn_2Mo_3O_8$ film.

Figure 3-6 shows the cross-sectional high-angle annular dark-field (HAADF)-STEM image of the film, where the electron beam was irradiated along the *a*-axis. From the image, four kinds of cation sites can be observed. The brightest and second brightest spots correspond to Mo sites, while darker spots represent Mn sites. Figure 3-6(b) shows the vertical intensity profiles along with line A and line B drawn in Fig. 3-6(a). The *z* positions of *tetra*-Mn and *octa*-Mn ions measured from the Mo ions ($z_{tetra\text{-Mn}}$ and $z_{octa\text{-Mn}}$) were approximately 2.11 and 2.58 Å, respectively (Fig. 3-6(c)). In $Mn_2Mo_3O_8$, the structural polarization (*P*') is less contributed by the Mo_3O_8 layers, and thus *P*' can be roughly evaluated from the *z* position of Mn ions as $P' = q_{Mn} \times [(z_{tetra\text{-Mn}} - c/4) + (z_{octa\text{-Mn}} - c/4)] / V_{f.u.} = q_{Mn} \times [2 \times z_{Mn\text{-center}}/c - 1/2] / S_{f.u.}$, where q_{Mn} is the charge of Mn ions, $z_{Mn\text{-center}}$ is the *z* position between *tetra*-Mn and *octa*-Mn, and $V_{f.u}$ and $S_{f.u.}$ are the volume and the bottom area of formula unit cell, respectively. The $z_{Mn\text{-center}}/c$ was estimated directly from the HAADF-STEM image. The estimated *P*' value of the film is 8.4±0.9 μC/cm^2, which is slightly larger than that of bulk (7.6 μC/cm^2) [70]. The increase of *P*' via tensile strain is predicted by DFT calculations (Fig. 3-7). Figure 3-6(d,e) shows STEM-energy dispersive X-ray spectrometry (EDX) images for Mo *L*-edge and Mn *K*-edge, revealing that Mo and Mn ions are located at the Mo and Mn sites, respectively. Figure 3-6(f) shows histograms of Mn *K* peak intensities for *tetra*-Mn and *octa*-Mn. The average peak intensity of *tetra*-Mn is almost equivalent to that of *octa*-Mn. In addition, XAS measurements revealed that Mo and Mn have valences of 4+ and 2+, respectively (Fig. 3-5). From these results, I concluded that the amount of Mn spins at the tetrahedral sites is almost the same as that at the octahedral sites in the present $Mn_2Mo_3O_8$ film.

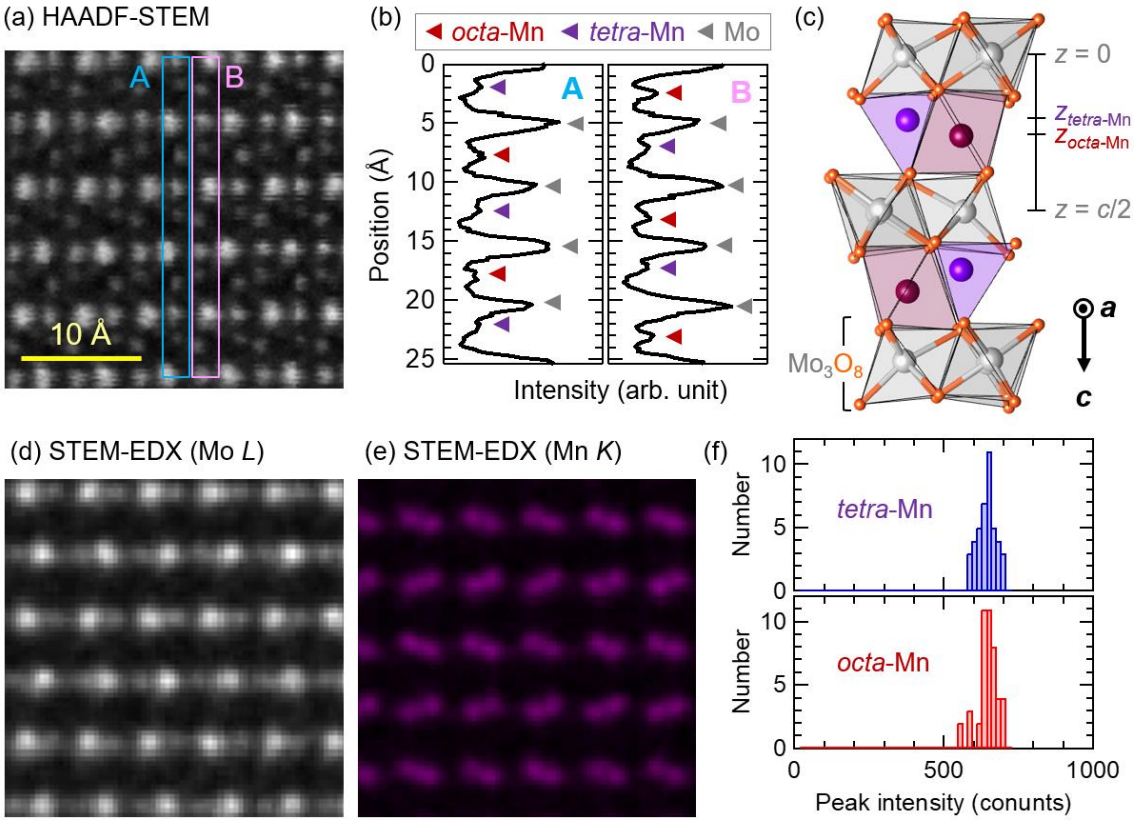

Figure 3-6. (a) HAADF-STEM image of the $Mn_2Mo_3O_8$ film and (b) vertical intensity profiles along with line A and line B in (a). (c) Crystal structure of $Mn_2Mo_3O_8$. STEM-EDX images at (d) Mo *L*-edge and (e) Mn *K*-edge. (f) Histogram of the Mn *K*-edge peak intensities for *tetra*-Mn and *octa*-Mn. Images (a), (d), and (e) were taken in the same area.

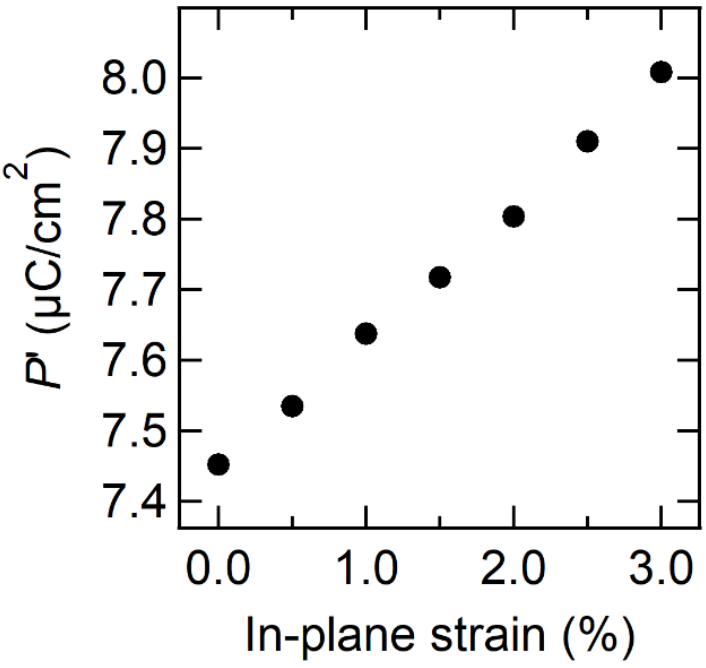

Figure 3-7. DFT-calculated *P'* values of $Mn_2Mo_3O_8$ as a function of in-plane strain.

3.3.2 Magnetic characterization

Figure 3-8(a) shows the in-plane and out-of-plane magnetization versus magnetic field (M–H) curves of the $Mn_2Mo_3O_8$ film at 2 K. In the in-plane measurement, H was applied along the a-axis. Magnetic hysteresis loops were observed in both curves, confirming the existence of magnetic order in the film. The in-plane remanent magnetization (M_r = 0.35 μ_B/f.u.) was more significant than the out-of-plane remanent magnetization (0.06 μ_B/f.u.), indicating in-plane magnetic anisotropy, which is in contrast to that in case of bulk $Mn_2Mo_3O_8$, with a magnet easy axis along the c-axis. The magnetic anisotropy coefficient of the film was calculated to be 5×10^5 erg/cm^3 at 2 K. The shape of the M–H curve is markedly different from that of bulk $Mn_2Mo_3O_8$; in bulk, M suddenly increases at H = 40 kOe from <0.01 to 0.5 μ_B/f.u. [2]. Figure 3-8(b) shows the in-plane and out-of-plane M versus temperature (T) curves of the $Mn_2Mo_3O_8$ film. The magnetic transition temperature (T_N) was evaluated to be 108 K, which is more than two times higher than that of bulk (41 K) [2]. T_N is also controllable by doping method; T_N for bulk $M_2Mo_3O_8$ with M = Mn, Fe, Co, and Ni is reported to be 41, 60, 39, and 6 K, respectively [27,32,33]. Compared to the doping method, the use of lattice strain seems more promising to enhance T_N. The lattice constants and magnetic properties of the $Mn_2Mo_3O_8$ film are summarized in Table 3-1.

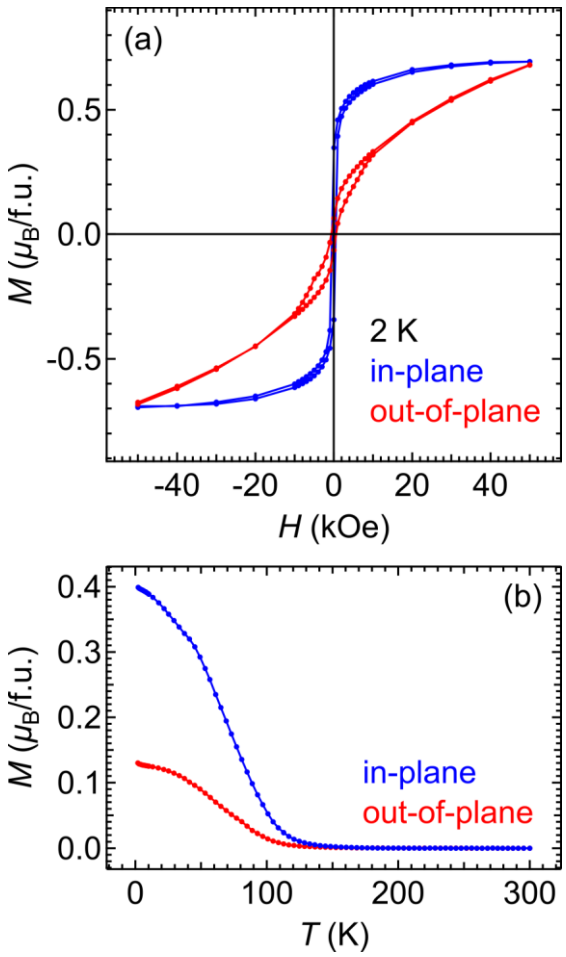

Figure 3-8. In-plane and out-of-plane (a) M–H curves at 2 K and (b) M–T curves under H = 500 Oe for the $Mn_2Mo_3O_8$ film.

Table 3-1. Lattice constants, magnet easy axis, M_r and M_s values at 2 K, the magnetic phase at 2 K, and T_N for the film and bulk $Mn_2Mo_3O_8$.

	Film [this study]	Bulk [2,70]
Lattice constants (Å)	a = 5.83 and c = 10.17	a = 5.8003 and c = 10.2425
M_r and M_s at 2 K (μ_B/f.u.)	0.35 and 0.70	1×10^{-2} and ~0.5
Magnetic phase transition at 2 K	No transition	FR–SF transition at 45 kOe
Magnetic easy axis	a-axis (in-plane)	c-axis
T_N (K)	108	41

3.3.3 Discussion of the magnetic phase of the $Mn_2Mo_3O_8$ film

The saturated magnetization (M_s) value of the film (0.7 μ_B/f.u.) was much smaller than that expected for ferromagnetic $Mn_2Mo_3O_8$ (~10 μ_B/f.u.) and comparable to that of bulk $Mn_2Mo_3O_8$ (~0.5 μ_B/f.u.) [2]. This suggests that similar to that in bulk, film $Mn_2Mo_3O_8$ undergoes antiferromagnetic interactions between *tetra*- and *octa*-Mn^{2+}. On the other hand, the M_r of the film (0.35 μ_B/f.u.) is much larger than that in case of the bulk (0.01 μ_B/f.u.) [2]. In bulk $Mn_2Mo_3O_8$, two magnetic phases appear at 2 K, depending on the H: FR phase at H < 45 kOe and SF phase at H > 45 kOe [2]. The small magnetization of the FR phase is derived from collinear antiferromagnetic ordering, while the non-collinear spin order leads to more significant magnetization in the SF phase, as illustrated in Fig. 3-1 [2]. Considering the enormous M_r value and the characteristic shape of the M−H curve, I conclude that the $Mn_2Mo_3O_8$ film does not undergo an H-induced magnetic phase transition at 2 K.

Here, I propose a non-collinear spin model responsible for the peculiar magnetic behavior of the $Mn_2Mo_3O_8$ film at low temperatures, as illustrated in Fig. 3-9(a). In the model, the magnetic moments of *tetra*- and *octa*-Mn^{2+} ions are canted from the *c*-axis with different orientations, resulting in a non-collinear spin order. Note that the most stable magnetic phase of bulk $Mn_2Mo_3O_8$ has a collinear spin configuration (Fig. 3-9(b)). The spontaneous magnetization of 0.35 μ_B/f.u. in the *a*-axis direction can be accounted for by assuming that the magnetic moment is inclined by 2° from the *c*-axis. Such epitaxial-strain-induced magnetic modulation is also observed in $BiFeO_3$; the non-collinear cycloidal spin structure changes into a canted G-type antiferromagnetic structure because of strains, resulting in the emergence of finite M_r [61].

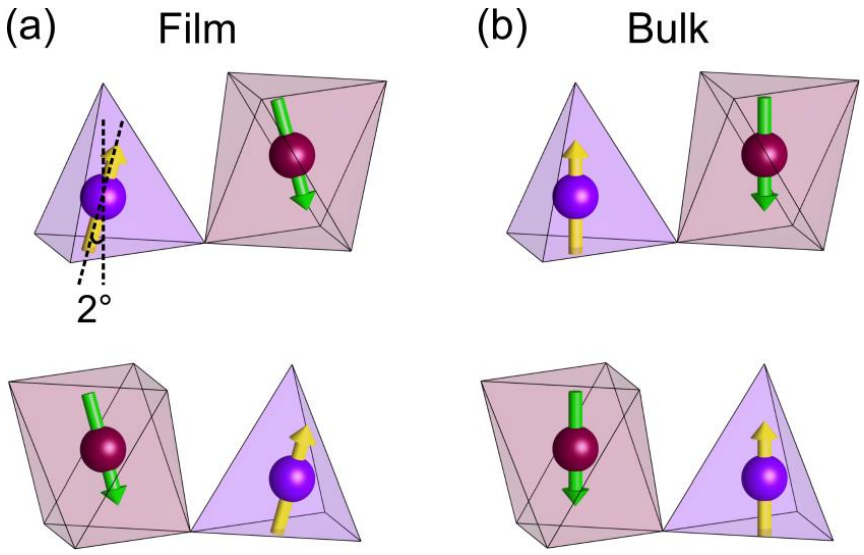

Figure 3-9. Schematic images of (a) a possible magnetic phase of the $Mn_2Mo_3O_8$ film and (b) the most stable magnetic phase of bulk $Mn_2Mo_3O_8$.

To investigate the origin of the non-collinear spin order in the $Mn_2Mo_3O_8$ film, I performed first-principles calculations for $Mn_2Mo_3O_8$ under tensile strain. Figure 3-10 shows nearest-neighbor exchange interaction (*J*), the strength of Dzyaloshinskii-Moriya (DM) interaction (*D*), and single-ion anisotropy (Δ_{tetra} and Δ_{octa} for *tetra*-Mn and *octa*-Mn, respectively) for $Mn_2Mo_3O_8$ as a function of in-plane strain calculated by using Xiang's approach [76]. The directions of the nearest-neighbor *tetra*-Mn^{2+} and *octa*-Mn^{2+} spins ($\vec{S}_{tetra}$ and $\vec{S}_{octa}$) can be evaluated from the following equation: $E_{\text{spin}} = J\vec{S}_{tetra} \cdot \vec{S}_{octa} + D \cdot (\vec{S}_{tetra} \times \vec{S}_{octa}) + \Delta_{tetra}(\vec{S}^z_{tetra})^2 + \Delta_{octa}(\vec{S}^z_{octa})^2$. As seen from Fig. 3-10, *D* was much smaller than others, indicating that the influence of DM interaction on the magnetism of $Mn_2Mo_3O_8$ is negligibly small. With increasing the in-plane strain, *J* monotonically decreased due to the increase of distance between the nearest-neighbor *tetra*-Mn^{2+} and *octa*-Mn^{2+} ions. Meanwhile, Δ_{tetra} and Δ_{octa} were less dependent on the strain. Notably, Δ_{tetra} and Δ_{octa} have positive and negative values, respectively, which is consistent with the previous calculation on unstrained $Mn_2Mo_3O_8$ [29]. Thus, if *J* is small

enough, $\vec{S}_{tetra}$ and $\vec{S}_{octa}$ are favored to be oriented in the in-plane and out-of-plane directions, respectively. Indeed, at 3 % in-plane strain, a noncollinear spin structure with an angle between $\vec{S}_{tetra}$ and $\vec{S}_{octa}$ of 1° becomes most stable, whereas collinear spin order is the most stable at 0 % strain. Consequently, a noncollinear spin structure can emerge in tensile-strained thin films due to opposite signs of single-ion anisotropies between *tetra*-Mn and *octa*-Mn and strain-induced decrease of *J*.

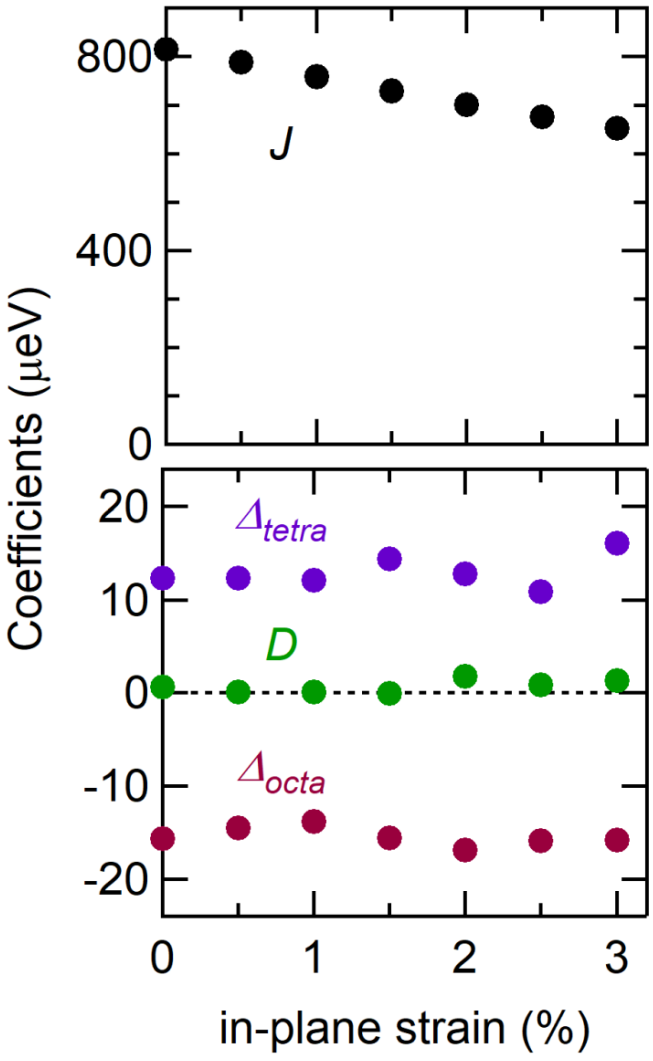

Figure 3-10. DFT-calculated *J*, *D*, Δ_{tetra} and Δ_{octa} values of $Mn_2Mo_3O_8$ as a function of in-plane strain.

3.4 Conclusion

In this study, I fabricated tensile-strained $Mn_2Mo_3O_8$ thin films on Al_2O_3(001) substrates. The valence states of Mn and Mo were divalent and tetravalent, respectively, similar to those of bulk $Mn_2Mo_3O_8$. The $Mn_2Mo_3O_8$ film exhibited a magnetic order with much larger M_r than in the case of bulk, suggesting the emergence of a non-collinear spin structure in which the magnetic moments were tilted from the *c*-axis through the epitaxial tensile strain. The remanent magnetization was aligned in the in-plane direction, in contrast to that in bulk $Mn_2Mo_3O_8$, supporting the non-collinear spin hypothesis. First-principles calculations suggest that the non-collinear spin structure is derived from opposite signs of single-ion anisotropies between *tetra*-Mn and *octa*-Mn and the strain-induced decrease of *J*.

4 Epitaxial strain control of crystal domains and magnetism of $Mn_2Mo_3O_8$ thin films

本章については、5 年以内に雑誌等で刊行予定のため、非公開。

5 Antisite-driven high-T_N ferrimagnetism in $Fe_2Mo_3O_8$ thin films

本章については、5 年以内に雑誌等で刊行予定のため、非公開。

6 General conclusion

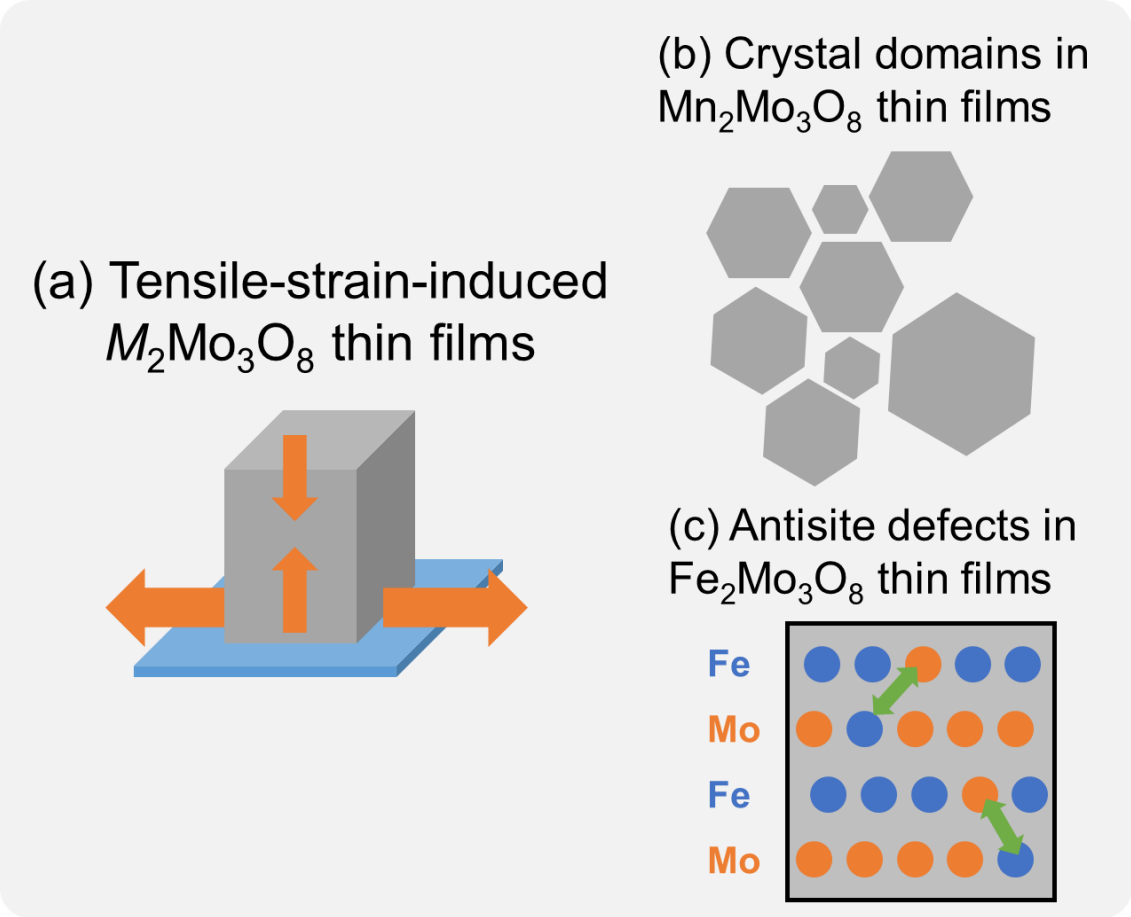

Figure 6-1. Schematic diagrams illustrating mechanisms of magnetism modulation by tensile strain. (a) Tensile strain and (b) control of crystal domains in $Mn_2Mo_3O_8$ thin films. (c) Antisite defects in $Fe_2Mo_3O_8$ thin films.

In this thesis, I experimentally and theoretically studied the magnetism of $M_2Mo_3O_8$ (M=Mn, Fe) epitaxial thin films. The investigation was accomplished through thin film fabrication, physical property characterization, and the first-principles calculation. With the achievements in this study, thin film fabrication is proved to be a powerful method to modulate the magnetism of $M_2Mo_3O_8$. Figure 6-1 summarizes the three factors for magnetism modulation in thin films. In both $Mn_2Mo_3O_8$ and $Fe_2Mo_3O_8$

thin films, tensile strain is induced, which affects the magnetism of $Fe_2Mo_3O_8$ thin films directly (Chapter 3). A variety of crystal domains is found in $Mn_2Mo_3O_8$ thin films (Chapter 4), while antisite defects are obtained in $Fe_2Mo_3O_8$ thin films (Chapter 5).

In Chapter 3, the tensile-strain effect on the magnetism of $Mn_2Mo_3O_8$ thin films on Al_2O_3(001) substrates was discussed. The $Mn_2Mo_3O_8$ film exhibited a magnetic order with much larger M_r than in the case of bulk, suggesting the emergence of a non-collinear spin structure in which the magnetic moments were tilted from the *c*-axis through the epitaxial tensile strain. The remanent magnetization was aligned in the in-plane direction, in contrast to that in bulk $Mn_2Mo_3O_8$, supporting the non-collinear spin hypothesis. First-principles calculations suggest that the non-collinear spin structure is derived from opposite signs of single-ion anisotropies between *tetra*-Mn and *octa*-Mn and the strain-induced decrease of *J*.

In Chapter 4, I fabricated $Mn_2Mo_3O_8$ films on YSZ(111) substrates. XRD and AFM measurements revealed that the films show island growth. The size of islands and the gap area between islands are dependent on the thickness of the films. The 100-nm-thick film with a larger average size of islands and a smaller gap area had a higher T_N of 163 K, which was much higher than those of the 35-nm-thick film on YSZ (122 K), 70-nm-thick film on Al_2O_3 (131 K), and bulk $Mn_2Mo_3O_8$ (41 K).

In Chapter 5, I fabricated tensile-strained $Fe_2Mo_3O_8$ thin films on Al_2O_3(001) and YSZ(111) substrates. The $Fe_2Mo_3O_8$ films exhibited an out-of-plane magnetic order with much larger M_r and H_C than in the case of bulk. XMCD measurements suggested that the sizeable finite magnetization emerged from the *tetra*-Fe^{2+} ions. The STEM-HAADF image suggested the occurrence of the antisite defects between *octa*-Fe and Mo. The first-principles calculations revealed that the structures with the antisite defects were stabilized

by tensile strain and the ferrimagnetism resulting from *tetra*-Fe was the most stable magnetic order, which supported the experimental results.

In conclusion, I successfully fabricated $M_2Mo_3O_8$ (M=Mn, Fe) epitaxial thin films and investigated the relationship between magnetism and tensile strain in detail. In the expanding research field of multiferroic oxide thin films, this achievement would provide a new perspective to design multiferroic materials with high practicality.

Appendix A. Band calculations of $Fe_2Mo_3O_8$

Band calculations based on DFT were performed using the Vienna ab initio simulation package [62–65]. The generalized gradient approximation by Perdew, Burke, and Ernzerhof was used for the exchange-correlation functional [66]. The localized natures of the *d* electrons in Fe and Mo were treated using the GGA+*U* method with *U* values of 4.0 and 3.0 eV for Fe and Mo, respectively [101]. The valence states, including $3p^6 3d^7 4s^1$ of Fe, $4s^2 4p^6 4d^5 5s^1$ of Mo, and $2s^2 2p^4$ of O, were described on a plane-wave basis with a cutoff energy of 700 eV. The other core electrons were considered by employing the projector augmented wave method [68,69]. Brillouin zone integration was performed using the Monkhorst–Pack scheme with a Γ-centered 3 × 3 × 2 **k**-point mesh for structure optimization [94] and Γ-centered 7 × 7 × 5 **k**-point mesh for electronic structure calculation. The ionic positions and lattice constants were optimized for both AFM- and ferrimagnetic (FR-) $Fe_2Mo_3O_8$ with spin-orbital coupling included such that the residual force on an atom and the pressure on the cell were smaller than 0.01 eV $Å^{-1}$ and 0.1 GPa, respectively. The crystal structures were visualized using VESTA [28].

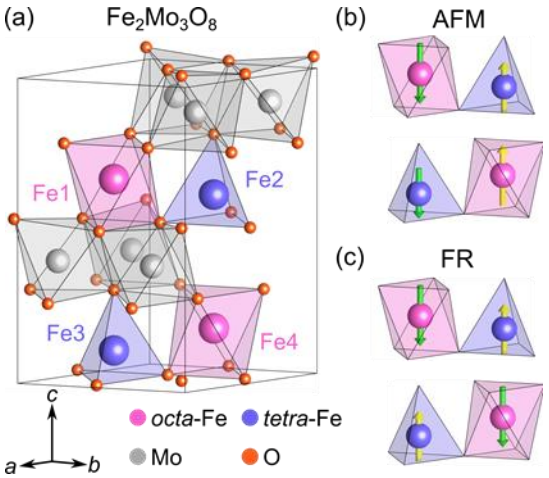

Figure A-1. (a) Crystal structure of hexagonal $Fe_2Mo_3O_8$ and spin order in (b) antiferromagnetic (AFM) and (c) ferrimagnetic (FR) phases.

The present DFT calculations including spin-orbital coupling revealed that both AFM- and FR-$Fe_2Mo_3O_8$ exhibited hexagonal symmetry, in contrast to a previous calculation without spin-orbital coupling predicting triclinic symmetry for both the AFM and FR phases [31]. The obtained *c*/*a* ratio of the AFM phase was consistent with the experimental value, 1.74 [36], confirming the reliability of the present calculations. The AFM phase was energetically more stable than the FR phase by 12.2 meV, consistent with the experimental reports. In both the AFM and FR phases, the *tetra*- and *octa*-Fe ions indicated a Fe^{2+} $3d^6$ high-spin state (S = 2). Furthermore, the magnetic moments of Fe ions were aligned along the *c*-axis, indicating uniaxial magnetic anisotropy along the c-axis.

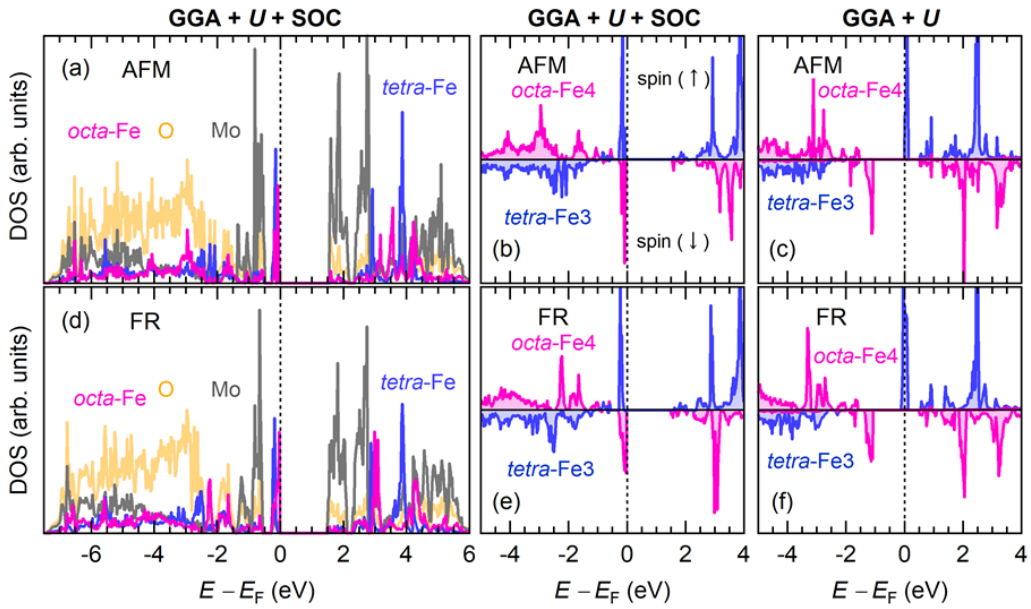

Figure A-2. Partial DOS spectra of (a,b) AFM- and (d,e) FR-$Fe_2Mo_3O_8$ calculated with SOC and (c,f) those without spin-orbital coupling. Pink, blue, gray, and yellow lines correspond to partial DOS of *octa*-Fe, *tetra*-Fe, Mo, and O ions, respectively.

Figure 2(a) depicts the density of states (DOS) profiles of AFM-$Fe_2Mo_3O_8$, indicating an insulating feature, as experimentally reported [31]. The valence band

maximum primarily comprised Fe 3*d* orbitals at both *tetra*- and *octa*-Fe, whereas the conduction band minimum was dominated by Mo 4*d* orbitals hybridized with O 2*p*. Note Mo singlet trimers form molecular bands as illustrated in Figure A-3, which can be classified as bonding (at around −1 eV in Fig. A-2), nonbonding (at around 1.8 eV), and antibonding (at around 2.5 eV) [25]. Figure A-2(b) shows the spin-resolved DOS spectra of the *octa*-Fe4 and *tetra*-Fe3 ions in Fig. A-1(a) near the Fermi energy (E_F). The magnetic moments of the *octa*-Fe4 and *tetra*-Fe3 ions were aligned antiparallel (spin-down) and parallel (spin-up) to the *c*-axis, respectively, as illustrated in Fig. A-1(b). Because the Fe^{2+} ions exhibited a high-spin state, the 3*d* orbitals of the *octa*-Fe4 (*tetra*-Fe3) ions accommodated five spin-down (spin-up) and one spin-up (spin-down) electrons. The energy levels of the former five electrons were located > 1 eV below E_F, whereas the latter one electron constituted states at $E - E_F$ = –0.3–0 eV. For comparison, I calculated the DOS of hexagonal AFM-$Fe_2Mo_3O_8$ without spin-orbital energy. As shown in Fig. A-2(c), the spectrum of the *tetra*-Fe3 ion has a finite DOS at E_F, unlike that with spin-orbital coupling (Fig. A-2(b)) [37].

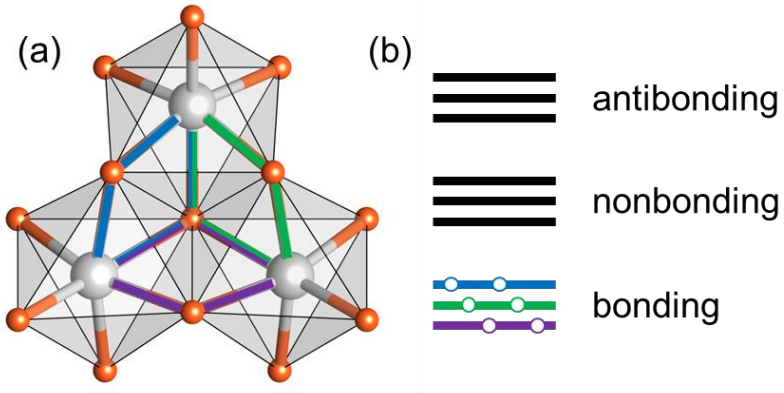

Figure A-3. (a) Formation of molecular orbitals in the Mo_3O_{13} cluster with the notations of Mo-O-Mo paths which bridge the hybridization bewteen 4*d* orbitals in each of the Mo-Mo bonds. (b) Schematic view of the band splitting in the cluster resulting in the nonmagnetic state, where six 4*d* electrons of Mo_3 reside at the bonding molecular orbitals [25].

Bibliography

[1] T. Ideue, T. Kurumaji, S. Ishiwata, and Y. Tokura, *Nat. Mater.* **16**, 797 (2017).

[2] T. Kurumaji, S. Ishiwata, and Y. Tokura, *Phys. Rev. B* **95**, 045142 (2017).

[3] H. Schmid, *Ferroelectrics* **162**, 317 (1994).

[4] N. a. Hill, *J. Phys. Chem. B* **104**, 6694 (2000).

[5] D. Khomskii, *Physics (College. Park. Md).* **2**, 20 (2009).

[6] J. A. Mundy, C. M. Brooks, M. E. Holtz, J. A. Moyer, H. Das, A. F. Rébola, J. T. Heron, J. D. Clarkson, S. M. Disseler, Z. Liu, A. Farhan, R. Held, R. Hovden, E. Padgett, Q. Mao, H. Paik, R. Misra, L. F. Kourkoutis, E. Arenholz, A. Scholl, J. A. Borchers, W. D. Ratcliff, R. Ramesh, C. J. Fennie, P. Schiffer, D. A. Muller, and D. G. Schlom, *Nature* **537**, 523 (2016).

[7] Y. Wu, J. Li, H. Huang, H. Bai, Y. Hong, K. Shi, and Z. Zhou, *Ceram. Int.* **43**, 13013 (2017).

[8] J. Wang, J. B. Neaton, H. Zheng, V. Nagarajan, S. B. Ogale, B. Liu, D. Viehland, V. Vaithyanathan, D. G. Schlom, U. V. Waghmare, N. A. Spaldin, K. M. Rabe, M. Wuttig, and R. Ramesh, *Science (80-.).* **299**, 1719 (2003).

[9] J. H. Lee, L. Fang, E. Vlahos, X. Ke, Y. W. Jung, L. F. Kourkoutis, J. W. Kim, P. J. Ryan, T. Heeg, M. Roeckerath, V. Goian, M. Bernhagen, R. Uecker, P. C. Hammel, K. M. Rabe, S. Kamba, J. Schubert, J. W. Freeland, D. A. Muller, C. J. Fennie, P. Schiffer, V. Gopalan, E. Johnston-Halperin, and D. G. Schlom, *Nat. 2010 4667309* **466**, 954 (2010).

[10] B. B. Van Aken, T. T. M. Palstra, A. Filippetti, and N. a Spaldin, *Nat. Mater.* **3**, 164 (2004).

[11] C. Lu, M. Wu, L. Lin, and J.-M. Liu, *Natl. Sci. Rev.* **6**, 653 (2019).

[12] T. Kimura, T. Goto, H. Shintani, K. Ishizaka, T. Arima, and Y. Tokura, *Nature* **426**, 55 (2003).

[13] X. Xu and W. Wang, *Mod. Phys. Lett. B* **28**, 1430008 (2014).

[14] R. S. P N, S. Mishra, and S. Athinarayanan, *APL Mater.* **8**, 040906 (2020).

[15] J. M. Rondinelli, A. S. Eidelson, and N. A. Spaldin, *Phys. Rev. B* **79**, 205119 (2009).

[16] H. Sakai, J. Fujioka, T. Fukuda, D. Okuyama, D. Hashizume, F. Kagawa, H. Nakao, Y. Murakami, T. Arima, A. Q. R. Baron, Y. Taguchi, and Y. Tokura, *Phys. Rev. Lett.* **107**, 137601 (2011).

[17] S. Dong, H. Xiang, and E. Dagotto, *Natl. Sci. Rev.* **6**, 629 (2019).

[18] I. E. Dzyaloshinskii, *JETP* **10**, 628 (1959).

[19] T. Moriya, *Phys. Rev.* **120**, 91 (1960).

[20] B. Lorenz, Y. Q. Wang, and C. W. Chu, *Phys. Rev. B - Condens. Matter Mater. Phys.* **76**, 104405 (2007).

[21] S. D. Kaushik, S. Rayaprol, J. Saha, N. Mohapatra, V. Siruguri, P. D. Babu, S. Patnaik, and E. V. Sampathkumaran, *J. Appl. Phys.* **108**, 084106 (2010).

[22] H. Murakawa, Y. Onose, S. Miyahara, N. Furukawa, and Y. Tokura, *Phys. Rev. Lett.* **105**, 137202 (2010).

[23] W. H. McCarroll, L. Katz, and R. Ward, *J. Am. Chem. Soc.* **79**, 5410 (1957).

[24] P. Strobel and Y. Le Page, *J. Cryst. Growth* **61**, 329 (1983).

[25] I. V Solovyev and S. V Streltsov, *Phys. Rev. Mater.* **3**, 114402 (2019).

[26] T. Kurumaji, S. Ishiwata, and Y. Tokura, *Phys. Rev. X* **5**, 031034 (2015).

[27] J. R. Morey, A. Scheie, J. P. Sheckelton, C. M. Brown, and T. M. McQueen, *Phys. Rev. Mater.* **3**, 014410 (2019).

[28] K. Momma and F. Izumi, *J. Appl. Crystallogr.* **44**, 1272 (2011).

[29] D. Szaller, K. Szász, S. Bordács, J. Viirok, T. Rõõm, U. Nagel, A. Shuvaev, L. Weymann, A. Pimenov, A. A. Tsirlin, A. Jesche, L. Prodan, V. Tsurkan, and I. Kézsmárki, *Phys. Rev. B* **102**, 144410 (2020).

[30] S. P. McAlister and P. Strobel, *J. Magn. Magn. Mater.* **30**, 340 (1983).

[31] Y. Wang, G. L. Pascut, B. Gao, T. A. Tyson, K. Haule, V. Kiryukhin, and S.-W. Cheong, *Sci. Rep.* **5**, 12268 (2015).

[32] S. P. McAlister and P. Strobel, *J. Magn. Magn. Mater.* **30**, 340 (1983).

[33] Y. S. Tang, S. M. Wang, L. Lin, C. Li, S. H. Zheng, C. F. Li, J. H. Zhang, Z. B. Yan, X. P. Jiang, and J.-M. Liu, *Phys. Rev. B* **100**, 134112 (2019).

[34] Y. S. Tang, J. H. Zhang, L. Lin, R. Chen, J. F. Wang, S. H. Zheng, C. Li, Y. Y. Zhang, G. Z. Zhou, L. Huang, Z. B. Yan, X. M. Lu, D. Wu, X. K. Huang, X. P. Jiang, and J.-M. Liu, *Phys. Rev. B* **103**, 014112 (2021).

[35] H. W. At and A. N. Abe, *Prog. Theor. Phys.* **18**, 405 (1957).

[36] Y. Kanazawa and A. Sasaki, *Acta Crystallogr. Sect. C Cryst. Struct. Commun.* **42**, 9 (1986).

[37] S. Reschke, A. A. Tsirlin, N. Khan, L. Prodan, V. Tsurkan, I. Kézsmárki, and J. Deisenhofer, *Phys. Rev. B* **102**, 094307 (2020).

[38] S. K. Kang, H. Tang, and T. A. Albright, *J. Am. Chem. Soc.* **115**, 1971 (1993).

[39] R. O. Kuzian, A. M. Daré, P. Sati, and R. Hayn, *Phys. Rev. B* **74**, 155201 (2006).

[40] C. Ederer and N. A. Spaldin, *Phys. Rev. B - Condens. Matter Mater. Phys.* **71**,

060401 (2005).

[41] A. Haykal, J. Fischer, W. Akhtar, J. Y. Chauleau, D. Sando, A. Finco, F. Godel, Y. A. Birkhölzer, C. Carrétéro, N. Jaouen, M. Bibes, M. Viret, S. Fusil, V. Jacques, and V. Garcia, *Nat. Commun. 2020 111* **11**, 1 (2020).

[42] Y. Yokoyama, Y. Yamasaki, M. Taguchi, Y. Hirata, K. Takubo, J. Miyawaki, Y. Harada, D. Asakura, J. Fujioka, M. Nakamura, H. Daimon, M. Kawasaki, Y. Tokura, and H. Wadati, *Phys. Rev. Lett.* **120**, 206402 (2018).

[43] G. Zhou, X. Wang, H. Ji, J. Zhang, P. Kang, Z. Li, and X. Xu, *J. Magn. Magn. Mater.* **515**, 167303 (2020).

[44] A. Beiranvand, E. Rivasto, H. Huhtinen, and P. Paturi, *ACS Omega* **6**, 34572 (2021).

[45] R. C. Sahoo, Y. Takeuchi, A. Ohtomo, and Z. Hossain, *Phys. Rev. B* **100**, 214436 (2019).

[46] A. K. Singh, S. Chauhan, S. K. Srivastava, and R. Chandra, *Solid State Commun.* **242**, 74 (2016).

[47] O. El Rhazouani, A. Benyoussef, Z. Zarhri, and A. El Kenz, *J. Magn. Magn. Mater.* **401**, 897 (2016).

[48] M. Nasir, M. Khan, S. Kumar, S. Bhatt, N. Patra, D. Bhattacharya, S. N. Jha, S. Biring, and S. Sen, *J. Magn. Magn. Mater.* **483**, 114 (2019).

[49] M. García-Hernández, J. L. Martínez, M. J. Martínez-Lope, M. T. Casais, and J. A. Alonso, *Phys. Rev. Lett.* **86**, 2443 (2001).

[50] K. I. Kobayashi, T. Kimura, H. Sawada, K. Terakura, and Y. Tokura, *Nat. 1998 3956703* **395**, 677 (1998).

[51] M. Saloaro, M. Hoffmann, W. A. Adeagbo, S. Granroth, H. Deniz, H. Palonen, H. Huhtinen, S. Majumdar, P. Laukkanen, W. Hergert, A. Ernst, and P. Paturi, *ACS Appl. Mater. Interfaces* **8**, 20440 (2016).

[52] S. Yamashita, J. Kikkawa, K. Yanagisawa, T. Nagai, K. Ishizuka, and K. Kimoto, *Sci. Rep.* **8**, 12325 (2018).

[53] P. Hohenberg and W. Kohn, *Phys. Rev.* **136**, B864 (1964).

[54] W. Kohn and L. J. Sham, *Phys. Rev.* **140**, 932 (1965).

[55] D. C. Langreth and M. J. Mehl, *Phys. Rev. B* **28**, 1809 (1983).

[56] J. F. Janak, *Phys. Rev. B* **18**, 7165 (1978).

[57] M. Cococcioni and S. de Gironcoli, *Phys. Rev. B* **71**, 035105 (2005).

[58] M. Born and R. Oppenheimer, *Ann. Phys.* **389**, 457 (1927).

[59] R. P. Feynman, *Phys. Rev.* **56**, 340 (1939).

[60] T. Ideue, T. Kurumaji, S. Ishiwata, and Y. Tokura, *Nat. Mater.* **16**, 797 (2017).

[61] D. Sando, A. Agbelele, D. Rahmedov, J. Liu, P. Rovillain, C. Toulouse, I. C. Infante, A. P. Pyatakov, S. Fusil, E. Jacquet, C. Carrétéro, C. Deranlot, S. Lisenkov, D. Wang, J.-M. Le Breton, M. Cazayous, A. Sacuto, J. Juraszek, A. K. Zvezdin, L. Bellaiche, B. Dkhil, A. Barthélémy, and M. Bibes, *Nat. Mater.* **12**, 641 (2013).

[62] G. Kresse and J. Hafner, *Phys. Rev. B* **47**, 558 (1993).

[63] G. Kresse and J. Hafner, *Phys. Rev. B* **49**, 14251 (1994).

[64] G. Kresse and J. Furthmiiller, *Comput. Mater. Sci.* **6**, 15 (1996).

[65] G. Kresse and J. Furthmüller, *Phys. Rev. B* **54**, 11169 (1996).

[66] J. P. Perdew, K. Burke, and M. Ernzerhof, *Phys. Rev. Lett.* **77**, 3865 (1996).

[67] G. Hautier, S. P. Ong, A. Jain, C. J. Moore, and G. Ceder, *Phys. Rev. B* **85**, 155208 (2012).

[68] P. E. Blöchl, *Phys. Rev. B* **50**, 17953 (1994).

[69] G. Kresse and D. Joubert, *Phys. Rev. B* **59**, 1758 (1999).

[70] H. Abe, A. Sato, N. Tsujii, T. Furubayashi, and M. Shimoda, *J. Solid State Chem.* **183**, 379 (2010).

[71] Z. K. Tang, M. Kawasaki, A. Ohtomo, H. Koinuma, and Y. Segawa, *J. Cryst. Growth* **287**, 169 (2006).

[72] R. Takahashi, H. Misumi, T. Yamamoto, and M. Lippmaa, *Cryst. Growth Des.* **14**, 1264 (2014).

[73] W. Dizayee, M. Ying, J. Griffin, M. S. Alqahtani, A. Buckley, A. M. Fox, and G. A. Gehring, *AIP Adv.* **8**, 055118 (2018).

[74] S. Nemrava, D. A. Vinnik, Z. Hu, M. Valldor, C.-Y. Kuo, D. A. Zherebtsov, S. A. Gudkova, C.-T. Chen, L. H. Tjeng, and R. Niewa, *Inorg. Chem.* **56**, 3861 (2017).

[75] A. N. Vasiliev, O. S. Volkova, L. S. Lobanovskii, I. O. Troyanchuk, Z. Hu, L. H. Tjeng, D. I. Khomskii, H.-J. Lin, C. T. Chen, N. Tristan, F. Kretzschmar, R. Klingeler, and B. Büchner, *Phys. Rev. B* **77**, 104442 (2008).

[76] H. J. Xiang, E. J. Kan, S.-H. Wei, M.-H. Whangbo, and X. G. Gong, *Phys. Rev. B* **84**, 224429 (2011).

[77] Y. Sun, X. Hu, W. Luo, and Y. Huang, *J. Mater. Chem.* **21**, 17229 (2011).

[78] B. Das, M. V. Reddy, C. Krishnamoorthi, S. Tripathy, R. Mahendiran, G. V. S. Rao, and B. V. R. Chowdari, *Electrochim. Acta* **54**, 3360 (2009).

[79] B. Lippold, J. Herrmann, W. Reichelt, and H. Oppermann, *Phys. Status Solidi* **121**, K91 (1990).

[80] L. Zhang, K. Shen, W. He, Y. Liu, L. Yin, and S. Guo, *J. Phys. Chem. Solids*

121, 71 (2018).

[81] S. Mo, T. Katayama, A. Chikamatsu, M. Kitamura, K. Horiba, H. Kumigashira, and T. Hasegawa, *Chem. Mater.* **33**, 7713 (2021).

[82] M. Ning, J. Li, C. K. Ong, and S. J. Wang, *J. Appl. Phys.* **103**, 013911 (2008).

[83] J. Jin, S. Ohkoshi, and K. Hashimoto, *Adv. Mater.* **16**, 48 (2004).

[84] D. Givord, P. Tenaud, and T. Viadieu, *J. Magn. Magn. Mater.* **72**, 247 (1988).

[85] D. Elbaz, D. Givord, S. Hirosawa, F. P. Missell, M. F. Rossignol, and V. Villas-Boas, *J. Appl. Phys.* **69**, 5492 (1991).

[86] S. Farokhipoor, C. Magén, S. Venkatesan, J. Íñiguez, C. J. M. Daumont, D. Rubi, E. Snoeck, M. Mostovoy, C. de Graaf, A. Müller, M. Döblinger, C. Scheu, and B. Noheda, *Nature* **515**, 379 (2014).

[87] T. Katayama, A. Chikamatsu, Y. Zhang, S. Yasui, H. Wadati, and T. Hasegawa, *Chem. Mater.* **33**, 5675 (2021).

[88] D. Szaller, K. Szász, S. Bordács, J. Viirok, T. Rõõm, U. Nagel, A. Shuvaev, L. Weymann, A. Pimenov, A. A. Tsirlin, A. Jesche, L. Prodan, V. Tsurkan, and I. Kézsmárki, *Phys. Rev. B* **102**, 144410 (2020).

[89] C. Gong, L. Li, Z. Li, H. Ji, A. Stern, Y. Xia, T. Cao, W. Bao, C. Wang, Y. Wang, Z. Q. Qiu, R. J. Cava, S. G. Louie, J. Xia, and X. Zhang, *Nature* **546**, 265 (2017).

[90] B. Huang, G. Clark, E. Navarro-Moratalla, D. R. Klein, R. Cheng, K. L. Seyler, Di. Zhong, E. Schmidgall, M. A. McGuire, D. H. Cobden, W. Yao, D. Xiao, P. Jarillo-Herrero, and X. Xu, *Nature* **546**, 270 (2017).

[91] X. G. Zheng, C. N. Xu, K. Nishikubo, K. Nishiyama, W. Higemoto, W. J. Moon, E. Tanaka, and E. S. Otabe, *Phys. Rev. B - Condens. Matter Mater. Phys.* **72**, 014464 (2005).

[92] B. J. Park, H. Han, J. Kim, Y. J. Kim, C. S. Kim, and B. W. Lee, *J. Magn. Magn. Mater.* **272**–**276**, 1851 (2004).

[93] A. Kumar, K. Klyukin, S. Ning, C. Ozsoy-Keskinbora, M. Ovsyanko, F. Van Uden, R. Krijnen, B. Yildiz, C. A. Ross, J. M. Lebeau, A. Kumar, K. Klyukin, S. Ning, +] B Yildiz, C. A. Ross, J. M. Lebeau, C. Ozsoy-Keskinbora, M. Ovsyanko, F. Van Uden, R. Krijnen, and B. Yildiz, *Adv. Funct. Mater.* 2107017 (2021).

[94] H. J. Monkhorst and J. D. Pack, *Phys. Rev. B* **13**, 5188 (1976).

[95] C. T. Chen, Y. U. Idzerda, H. J. Lin, N. V. Smith, G. Meigs, E. Chaban, G. H. Ho, E. Pellegrin, and F. Sette, *Phys. Rev. Lett.* **75**, 152 (1995).

[96] J. Y. Kim, T. Y. Koo, and J. H. Park, *Phys. Rev. Lett.* **96**, 047205 (2006).

[97] T. J. Regan, H. Ohldag, C. Stamm, F. Nolting, J. Lüning, J. Stöhr, and R. L. White, *Phys. Rev. B* **64**, 214422 (2001).

[98] Y. K. Wakabayashi, Y. Nonaka, Y. Takeda, S. Sakamoto, K. Ikeda, Z. Chi, G. Shibata, A. Tanaka, Y. Saitoh, H. Yamagami, M. Tanaka, A. Fujimori, and R. Nakane, *Phys. Rev. B* **96**, 104410 (2017).

[99] K. Matsuura, H. Sagayama, Y. Nii, N. D. Khanh, N. Abe, and T. Arima, *Phys. Rev. B - Condens. Matter Mater. Phys.* **92**, 035133 (2015).

[100] S. P. Ong, W. D. Richards, A. Jain, G. Hautier, M. Kocher, S. Cholia, D. Gunter, V. L. Chevrier, K. A. Persson, and G. Ceder, *Comput. Mater. Sci.* **68**, 314 (2013).

[101] S. L. Dudarev, G. A. Botton, S. Y. Savrasov, C. J. Humphreys, and A. P. Sutton, *Phys. Rev. B* **57**, 1505 (1998).